

Combined analysis of effective Higgs portal dark matter models

Ankit Beniwal,^{1,*} Filip Rajec,^{1,†} Christopher Savage,^{2,3,‡} Pat Scott,^{4,§}

Christoph Weniger,^{5,¶} Martin White,^{1,**} and Anthony G. Williams^{1,††}

¹*ARC Center of Excellence for Particle Physics at the Terascale & CSSM,
Department of Physics, University of Adelaide, Adelaide, SA 5005, Australia*

²*Nordita, KTH Royal Institute of Technology and Stockholm University, Stockholm, Sweden*

³*Department of Physics & Astronomy, University of Utah, Salt Lake City, Utah, USA*

⁴*Department of Physics, Imperial College London, Blackett Laboratory,
Prince Consort Road, London SW7 2AZ, United Kingdom*

⁵*GRAPPA, University of Amsterdam, Science Park 904, 1090 GL Amsterdam, Netherlands*

(Dated: December 8, 2024)

We combine and extend the analyses of effective scalar, vector, Majorana and Dirac fermion Higgs portal models of Dark Matter (DM), in which DM couples to the Standard Model (SM) Higgs boson via an operator of the form $\mathcal{O}_{\text{DM}} H^\dagger H$. For the fermion models, we take an admixture of scalar $\bar{\psi}\psi$ and pseudoscalar $\bar{\psi}i\gamma_5\psi$ interaction terms. For each model, we apply constraints on the parameter space based on the Planck measured DM relic density and the LHC limits on the Higgs invisible branching ratio. For the first time, we perform a consistent study of the indirect detection prospects for these models based on the WMAP7/Planck observations of the CMB, a combined analysis of 15 dwarf spheroidal galaxies by Fermi-LAT and the upcoming Cherenkov Telescope Array (CTA). We also perform a correct treatment of the momentum-dependent direct search cross-section that arises from the pseudoscalar interaction term in the fermionic DM theories. We find, in line with previous studies, that current and future direct search experiments such as LUX and XENON1T can exclude much of the parameter space, and we demonstrate that a joint observation in both indirect and direct searches is possible for high mass WIMPs. In the case of a pure pseudoscalar interaction of a fermionic DM candidate, future gamma-ray searches are the only class of experiment capable of probing the high mass range of the theory.

* Electronic address: ankit.beniwal@adelaide.edu.au

† Electronic address: filip.rajec@adelaide.edu.au

‡ Electronic address: chris@savage.name

§ Electronic address: p.scott@imperial.ac.uk

¶ Electronic address: c.weniger@uva.nl

** Electronic address: martin.white@adelaide.edu.au

†† Electronic address: anthony.williams@adelaide.edu.au

I. INTRODUCTION

Evidence for Dark Matter (DM) in our universe has been accumulating for decades [1]. As none of the particles of the Standard Model (SM) adequately explains a wide range of astrophysical observations of DM, we are forced to look for viable candidates in theories that lie Beyond the SM (BSM). It has been noted that a GeV-scale DM candidate can accurately reproduce the observed relic density of DM provided that it has a weak interaction cross-section, leading to the so-called “Weakly Interacting Massive Particle” (WIMP) miracle [2, 3].

Within the WIMP scenario, there are typically multiple complimentary experimental probes that exploit the couplings between the WIMP and SM fermions/gauge bosons. In addition, there are two primary theoretical approaches for specifying the SM-WIMP couplings. One is the top-down approach, where a WIMP is included amongst the new particle content of a BSM theory at high energies, and one can derive the WIMP interactions from the details of this new theory (e.g., supersymmetry with a neutralino WIMP). The other is the bottom-up approach in which effective field theories (EFT) are constructed from the lowest dimensional operators allowed in a weak-scale Lagrangian. In this approach, one assumes a DM-SM interaction Lagrangian of the form

$$\mathcal{L}_{\text{int}} \supset \Lambda^{-n} \mathcal{O}_{\text{DM}} \mathcal{O}_{\text{SM}}, \quad (1)$$

where Λ is the EFT cut-off scale and \mathcal{O}_{DM} (\mathcal{O}_{SM}) are the DM (SM) operators that are singlets under the SM gauge groups. An EFT ceases to be valid when the momentum transfer in an experimental process of interest approaches the interaction mediator mass. An option that has generated much interest in the literature is that in which the DM interacts with SM particles via a Higgs portal [4–35]. This is motivated partly by the simplicity of the model in terms of the required BSM particle content, and partly by the fact that the operator $H^\dagger H$ is one of the two lowest-dimensional gauge-invariant operators that one can write in the SM (the other being the hypercharge field strength tensor $B_{\mu\nu}$). The recent discovery of the Higgs boson by the ATLAS [36] and CMS [37] experiments of the Large Hadron Collider gives us an extra experimental window into the possible connections between the Higgs boson and DM.

In this paper, we revisit four simple effective field theories for Higgs portal dark matter, namely those in which the DM is assumed to be a scalar, vector or Majorana/Dirac fermion. For the fermion models, one may consider parity-conserving scalar couplings ($\mathcal{O}_{\text{DM}} \propto \bar{\psi}\psi$) and/or parity-violating pseudoscalar couplings ($\mathcal{O}_{\text{DM}} \propto \bar{\psi}i\gamma_5\psi$). There are a few omissions in the literature that make a new combined study of these scenarios worthwhile. The first is that most studies have not properly

summarised the impacts of current and future indirect search experiments on the parameter space of the models. In some cases (e.g., fermionic dark matter with scalar interactions) this is because the indirect signatures are velocity suppressed, whilst in others it has been assumed that the ability of direct detection to probe much of the parameter space renders indirect detection less important. We argue instead that it is vital to establish which regions of the model space are visible in multiple experiments, since this might ultimately present us with a much deeper understanding of the DM problem (e.g., one could imagine using a more detailed knowledge of the particle physics obtained in one experiment to better measure astrophysical factors such as the DM halo distribution, as proposed in [38]). With the approaching availability of the Cherenkov Telescope Array (CTA), it is an opportune moment to explore its expected reach. It is also the case that studies of the direct detection constraints on fermionic models have not always treated the momentum suppression of the direct detection cross-section correctly in the case of a pseudoscalar coupling. We remedy this in our study by rederiving the limits from the XENON100 and LUX experiments using a dedicated code that includes an accurate treatment of the momentum-dependent scattering cross-sections. Finally, we perform the same comprehensive study across all of the four models, and thus are able to present a consistent set of detailed results for the first time.

Our paper can be viewed as an extension of the scalar singlet DM model study presented in [39]. A global fit of the same model was presented in [40]. The scalar, vector and Majorana fermion Higgs portal models we consider have previously been studied in [41] in light of the WMAP, XENON100 as well as the Higgs invisible width and XENON1T prospects. Current LHC constraints from a CMS vector boson fusion analysis, and LHC monojet and mono-Z analyses are shown to be very weak for the scalar singlet DM model in [42]. Monojet constraints on all SM Higgs portal models (scalar, fermion and vector) are shown to be weak in [43]. Constraints on the parameter space of the scalar model from perturbativity and electroweak vacuum stability in the early Universe were imposed in [44]. The LUX limits on the scalar DM model were first considered in [45]. The same paper also evaluated limits from anti-proton data, which are shown to be important in the region of the Higgs resonance and competitive with the LUX limits at higher DM masses. For the fermion models, the corresponding anti-proton limits in scalar interactions are weak due to the velocity suppression of the annihilation cross-section σv_{rel} . In all cases, the results are strongly-dependent on the propagation model. The parity-conserving fermion DM case was considered in [41]. A combination of the parity-conserving and parity-violating terms were first considered in [46] and recently in [47] where it was noted that the parity-violating term can significantly generate a parity-conserving coupling after Electroweak Symmetry Breaking (EWSB).

We aim to provide a complete description of the current and projected future limits on the parameter space of the effective scalar, vector, Majorana and Dirac fermion models in this paper. For each model, we apply currently available constraints from the dark matter relic density, Higgs invisible width, indirect and direct detection limits. For the indirect searches, the current limits we impose come from the WMAP 7-year observations of the CMB (WMAP7) and a combined analysis of 15 dwarf galaxy observations by Fermi-LAT; for projected future limits, we use the Planck polarization data, projected improvements in Fermi dwarf galaxy observations and prospects for the planned CTA. Our direct detection data is taken from XENON100 (2012) and LUX (2013).

The paper is organised as follows. In Section II, we introduce our four Higgs portal models based on the DM spin. Section III contains a detailed description of the model constraints and their implementations. Our model results and their prospects for detection at current and/or future based experiments are presented in Section IV. Our conclusions are given in Section V. A detailed derivation of the physical mass basis required to understand the fermionic EFTs after EWSB is given in Appendix A.

II. MODELS

The DM fields are assumed to be SM gauge singlets. We consider four cases for the spin of the DM: scalar (S), vector (V_μ), Majorana (χ) and Dirac (ψ) fermion. Lagrangians for the corresponding DM fields, invariant under the symmetries of the SM, are¹

$$\mathcal{L}_S = \mathcal{L}_{\text{SM}} + \frac{1}{2}(\partial_\mu S)(\partial^\mu S) - \frac{1}{2}\mu_S^2 S^2 - \frac{1}{4!}\lambda_S S^4 - \frac{1}{2}\lambda_{hS} S^2 H^\dagger H, \quad (2)$$

$$\mathcal{L}_V = \mathcal{L}_{\text{SM}} - \frac{1}{4}W_{\mu\nu}W^{\mu\nu} + \frac{1}{2}\mu_V^2 V_\mu V^\mu - \frac{1}{4!}\lambda_V (V_\mu V^\mu)^2 + \frac{1}{2}\lambda_{hV} V_\mu V^\mu H^\dagger H, \quad (3)$$

$$\mathcal{L}_\chi = \mathcal{L}_{\text{SM}} + \frac{1}{2}\bar{\chi}(i\not{\partial} - \mu_\chi)\chi - \frac{1}{2}\frac{\lambda_{h\chi}}{\Lambda_\chi} \left(\cos\theta \bar{\chi}\chi + \sin\theta \bar{\chi}i\gamma_5\chi \right) H^\dagger H, \quad (4)$$

$$\mathcal{L}_\psi = \mathcal{L}_{\text{SM}} + \bar{\psi}(i\not{\partial} - \mu_\psi)\psi - \frac{\lambda_{h\psi}}{\Lambda_\psi} \left(\cos\theta \bar{\psi}\psi + \sin\theta \bar{\psi}i\gamma_5\psi \right) H^\dagger H, \quad (5)$$

where \mathcal{L}_{SM} is the SM Lagrangian, $W_{\mu\nu} \equiv \partial_\mu V_\nu - \partial_\nu V_\mu$ is the field-strength tensor of the vector field V_μ and H is the SM Higgs doublet. The parameter θ determines the type of interaction between DM and the Higgs field: $\cos\theta = 1$ corresponds to a pure scalar interaction and $\cos\theta = 0$ corresponds to a pure pseudoscalar interaction.

¹ We adopt our scalar and vector models from Ref. [9] with the following substitutions for **Scalar**: $\phi \rightarrow S$, $M_S \rightarrow \mu_S$, $c_S \rightarrow \lambda_{hS}$, $d_S \rightarrow \lambda_S$ and **Vector**: $V_{\mu\nu} \rightarrow W_{\mu\nu}$, $M_V \rightarrow \mu_V$, $c_V \rightarrow \lambda_{hV}$, $d_V \rightarrow \lambda_V$. The Dirac and Majorana models are taken instead from Ref. [47] with the following substitutions for **Dirac**: $\chi \rightarrow \psi$, $M_0 \rightarrow \mu_\psi$, $1/\Lambda \rightarrow -\lambda_{h\psi}/\Lambda_\psi$ and **Majorana**: $\chi \rightarrow \chi/\sqrt{2}$, $M_0 \rightarrow \mu_\chi$, $1/\Lambda \rightarrow -\lambda_{h\chi}/\Lambda_\chi$.

DM particles are required to be stable on cosmological time scales. For the models introduced above, their stability is guaranteed by imposing an assumed \mathcal{Z}_2 symmetry: $X \rightarrow -X$ for $X \in (S, V, \chi, \psi)$. Under the \mathcal{Z}_2 symmetry, the DM fields (S, V_μ, χ, ψ) are assumed to be *odd* while the SM fields are assumed to be *even*. The decay of a DM particle into SM particles is therefore forbidden. Furthermore, the imposed symmetry also prohibits linear and cubic terms in the scalar field Lagrangian as well as the kinetic mixing terms in the vector field-strength tensor $W_{\mu\nu}$. As an explicit bare mass term for the DM field is allowed by the \mathcal{Z}_2 symmetry, we have included it in our Lagrangians above for completeness.

The scalar model in Eq. (2) is the simplest extension of the SM and was first introduced 30 years ago [48]. It was later studied by the authors of Refs. [49, 50]. It is both theoretically and phenomenologically satisfactory as long as the \mathcal{Z}_2 symmetry remains unbroken. It is renormalizable and hence valid up to high energy scales as long as the Landau pole is not reached. The vector model in Eq. (3) is very simple, compact and appears renormalizable due of the presence of dim-2 and dim-4 operators only. However, in reality, it is non-renormalizable and violates unitarity (in a similar fashion to the four-fermion interaction of the pre-electroweak theory). Therefore, it is an effective model which needs to be UV-completed. UV-complete models will be the subject of future work and hence are considered to be beyond the scope of this study. Simple UV-completions can be found in Refs. [51, 52]. The Majorana and Dirac fermion models in Eqs. (4) and (5) respectively are also non-renormalizable, and a suggested UV completion can be found in Ref. [53].

After EWSB, the SM Higgs doublet acquires a Vacuum Expectation Value (VEV). In the unitary gauge, the SM Higgs doublet reduces to

$$H = \frac{1}{\sqrt{2}} \begin{pmatrix} 0 \\ v_0 + h \end{pmatrix} \quad (6)$$

where h is the physical SM Higgs field and $v_0 = 246.22$ GeV is the SM Higgs VEV. Consequently the $H^\dagger H$ term in above Lagrangians expands to

$$H^\dagger H = \frac{1}{2}v_0^2 + v_0h + \frac{1}{2}h^2 \quad (7)$$

which generates mass and interaction terms for the DM fields $X \in (S, V, \chi, \psi)$. After substituting

the expanded expression for $H^\dagger H$ into the above Lagrangians, we find

$$\mathcal{L}_S = \mathcal{L}_{\text{SM}} + \frac{1}{2}(\partial_\mu S)(\partial^\mu S) - \frac{1}{2}m_S^2 S^2 - \frac{1}{4!}\lambda_S S^4 - \frac{1}{2}\lambda_{hS} S^2 \left(v_0 h + \frac{1}{2}h^2\right), \quad (8)$$

$$\mathcal{L}_V = \mathcal{L}_{\text{SM}} - \frac{1}{4}W_{\mu\nu}W^{\mu\nu} + \frac{1}{2}m_V^2 V_\mu V^\mu - \frac{1}{4!}\lambda_V (V_\mu V^\mu)^2 + \frac{1}{2}\lambda_{hV} V_\mu V^\mu \left(v_0 h + \frac{1}{2}h^2\right), \quad (9)$$

$$\begin{aligned} \mathcal{L}_\chi = \mathcal{L}_{\text{SM}} + \frac{1}{2}\bar{\chi}i\not{\partial}\chi - \frac{1}{2}\left[\mu_\chi\bar{\chi}\chi + \frac{1}{2}\frac{\lambda_{h\chi}}{\Lambda_\chi}v_0^2\left(\cos\theta\bar{\chi}\chi + \sin\theta\bar{\chi}i\gamma_5\chi\right)\right] \\ - \frac{1}{2}\frac{\lambda_{h\chi}}{\Lambda_\chi}\left(\cos\theta\bar{\chi}\chi + \sin\theta\bar{\chi}i\gamma_5\chi\right)\left(v_0 h + \frac{1}{2}h^2\right), \end{aligned} \quad (10)$$

$$\begin{aligned} \mathcal{L}_\psi = \mathcal{L}_{\text{SM}} + \bar{\psi}i\not{\partial}\psi - \left[\mu_\psi\bar{\psi}\psi + \frac{1}{2}\frac{\lambda_{h\psi}}{\Lambda_\psi}v_0^2\left(\cos\theta\bar{\psi}\psi + \sin\theta\bar{\psi}i\gamma_5\psi\right)\right] \\ - \frac{\lambda_{h\psi}}{\Lambda_\psi}\left(\cos\theta\bar{\psi}\psi + \sin\theta\bar{\psi}i\gamma_5\psi\right)\left(v_0 h + \frac{1}{2}h^2\right), \end{aligned} \quad (11)$$

where the physical masses of the scalar and vector fields respectively are

$$\text{Scalar: } m_S^2 = \mu_S^2 + \frac{1}{2}\lambda_{hS}v_0^2, \quad \text{Vector: } m_V^2 = \mu_V^2 + \frac{1}{2}\lambda_{hV}v_0^2. \quad (12)$$

For the Majorana and Dirac models, we have non mass-type contributions that are purely quadratic in the DM fields when $\sin\theta \neq 0$. As explained in Appendix A, it is convenient to perform a chiral rotation and field redefinition after EWSB to have a properly defined real mass. The chiral rotation of the fields is given by

$$\begin{aligned} \text{Majorana: } \chi &\rightarrow \exp(i\gamma_5\alpha/2)\chi, \quad \bar{\chi} \rightarrow \bar{\chi}\exp(i\gamma_5\alpha/2), \\ \text{Dirac: } \psi &\rightarrow \exp(i\gamma_5\alpha/2)\psi, \quad \bar{\psi} \rightarrow \bar{\psi}\exp(i\gamma_5\alpha/2), \end{aligned} \quad (13)$$

where α is a real parameter, independent of space-time coordinates.

After substituting the redefined, rotated Majorana and Dirac fields from Eq. (13) into Eqs. (10) and (11), we demand the coefficients of the terms $\bar{\chi}i\gamma_5\chi$ and $\bar{\psi}i\gamma_5\psi$ to vanish in order to go to the real-mass basis. Consequently, this imposes a constraint on the allowed values of the parameter α . Using our derived results for the Dirac and Majorana models in Appendix A, the allowed values of the parameter α are

$$\tan\alpha = \left(-\frac{1}{2}\frac{\lambda_{h\chi,h\psi}}{\Lambda_{\chi,\psi}}v_0^2\sin\theta\right)\left(\mu_{\chi,\psi} + \frac{1}{2}\frac{\lambda_{h\chi,h\psi}}{\Lambda_{\chi,\psi}}v_0^2\cos\theta\right)^{-1}.$$

Consequently, the post-EWSB Lagrangians for the Majorana and Dirac models are

$$\mathcal{L}_\chi = \mathcal{L}_{\text{SM}} + \frac{1}{2}\bar{\chi}i\not{\partial}\chi - \frac{1}{2}m_\chi\bar{\chi}\chi - \frac{1}{2}\frac{\lambda_{h\chi}}{\Lambda_\chi}\left[\cos\xi\bar{\chi}\chi + \sin\xi\bar{\chi}i\gamma_5\chi\right]\left(v_0 h + \frac{1}{2}h^2\right), \quad (14)$$

$$\mathcal{L}_\psi = \mathcal{L}_{\text{SM}} + \bar{\psi}i\not{\partial}\psi - m_\psi\bar{\psi}\psi - \frac{\lambda_{h\psi}}{\Lambda_\psi}\left[\cos\xi\bar{\psi}\psi + \sin\xi\bar{\psi}i\gamma_5\psi\right]\left(v_0 h + \frac{1}{2}h^2\right), \quad (15)$$

where $\xi \equiv \theta + \alpha$ and

$$\cos \xi = \frac{\mu_\chi}{m_{\chi,\psi}} \left(\cos \theta + \frac{v_0^2}{2\mu_{\chi,\psi}} \frac{\lambda_{h\chi,h\psi}}{\Lambda_{\chi,\psi}} \right), \quad \sin \xi = \frac{\mu_{\chi,\psi}}{m_{\chi,\psi}} \sin \theta,$$

$$m_{\chi,\psi} = \sqrt{\left(\mu_{\chi,\psi} + \frac{1}{2} \frac{\lambda_{h\chi,h\psi}}{\Lambda_{\chi,\psi}} v_0^2 \cos \theta \right)^2 + \left(\frac{1}{2} \frac{\lambda_{h\chi,h\psi}}{\Lambda_{\chi,\psi}} v_0^2 \sin \theta \right)^2}.$$

The parameters m_χ and m_ψ are the physical masses of the Majorana (χ) and Dirac (ψ) DM fields respectively.

III. CONSTRAINTS

For the scalar and vector models after EWSB, the remaining free model parameters are the DM mass $m_{S,V}$ and its coupling $\lambda_{hS,hV}$ with the SM Higgs boson.² The Majorana and Dirac fermion models in Eqs. (14) and (15) respectively yield three model parameters: $\cos \xi$, $m_{\chi,\psi}$ and $\lambda_{h\chi,h\psi}/\Lambda_{\chi,\psi}$. For simplicity, we choose to keep the parameter $\cos \xi$ fixed when imposing fermion model constraints. More specifically, we study the cases when $\cos \xi = 1$ (pure scalar interaction), $\cos \xi = 1/\sqrt{2}$ (equally mixed scalar-pseudoscalar interaction) and $\cos \xi = 0$ (pure pseudoscalar interaction). Hence, the remaining free parameters in fermion models are the DM mass $m_{\chi,\psi}$ and its coupling $\lambda_{h\chi,h\psi}/\Lambda_{\chi,\psi}$ with the SM Higgs boson.³

As we impose identical sets of constraints on each model parameter space, we will instead refer to parameters m_X and λ_{hX} where $X \in (S, V, \chi, \psi)$. In situations where a given constraint is model specific, we impose those constraints on the model parameters directly.

A. Relic Density

Currently, the best known value of the DM relic density (or abundance) comes from the Planck satellite measurement of the Cosmic Microwave Background (CMB) temperature and lensing-potential power spectra [61]

$$\Omega_{\text{DM}} h^2 = 0.1199 \pm 0.0027, \quad (16)$$

where $\Omega_{\text{DM}} \equiv \rho_{\text{DM}}/\rho_c$ is the fraction of the DM mass density relative to the critical density $\rho_c = 3H_0^2/8\pi G$, and the parameter $h = H_0/(100 \text{ km sec}^{-1} \text{ Mpc}^{-1})$ is the reduced Hubble constant.

² For our analysis, we ignore the quartic self-coupling $\lambda_{S,V}$ since it plays no observable role in the dark matter phenomenology. However, they are important when the constraints from electroweak vacuum stability and model perturbativity are imposed (see e.g., Ref. [54–60].)

³ In the model Lagrangians from Eqs. (2) to (5), the scalar/vector DM coupling $\lambda_{hS,hV}$ has mass dimension M^0 while the Majorana/Dirac fermion DM coupling $\lambda_{h\chi,h\psi}/\Lambda_{\chi,\psi}$ has mass dimension M^{-1} .

In general, WIMPs in thermal equilibrium in the early Universe that annihilate purely via the s -channel have a relic density that varies inversely with the velocity-averaged annihilation cross-section $\langle\sigma v_{\text{rel}}\rangle$ through

$$\Omega_{\text{DM}} h^2 \sim \frac{3 \times 10^{-27} \text{ cm}^3 \text{ s}^{-1}}{\langle\sigma v_{\text{rel}}\rangle}. \quad (17)$$

Consequently, a smaller $\langle\sigma v_{\text{rel}}\rangle$ produces an *overabundance* of WIMPs whereas a larger $\langle\sigma v_{\text{rel}}\rangle$ produces an *underabundance* of WIMPs in the Universe today.

For our Higgs portal models, the model relic density is mostly determined by the Higgs-mediated s -channel annihilation into SM particles. A sub-dominant role is played by the annihilation into hh through the direct $h^2 X^2$ vertex as well as the Higgs-mediated t -channel annihilation of X . Since $\langle\sigma v_{\text{rel}}\rangle$ scales as the *square* of the SM Higgs-DM coupling λ_{hX} , larger (smaller) values of λ_{hX} lead to a suppressed (enhanced) relic density $\Omega_X h^2$ in agreement with Eq. (17).

We use the publicly available software `LanHEP3.2.0` [62, 63] to implement the scalar model in Eq. (2), vector model in Eq. (3) and the redefined, chiral-rotated Majorana and Dirac models in Eqs. (14) and (15) respectively.⁴ For the calculation of the relic density $\Omega_X h^2$, annihilation cross-section σv_{rel} and the gamma-ray yields per annihilation, we use `micrOMEGAs3.6.9.2` [64, 65] to automate calculations in each model.⁵ In computing the relic density, we also take into account the annihilation of DM into virtual gauge bosons.

The Planck measured relic density in Eq. (16) restricts the allowed values of the SM Higgs-DM coupling. For each of our models, we scan along the DM mass axis and for each mass, find the coupling that gives the correct relic density using Brent's method [66].⁶ These couplings are roots (or zeros) of the function

$$f_{\Omega}(m_X, \lambda_{hX}) = \Omega_{\text{DM}} h^2 - \Omega_X h^2, \quad (18)$$

where we take $\Omega_{\text{DM}} h^2 = 0.1199$ corresponding to the central value of Eq. (16) whereas $\Omega_X h^2$ is the model relic density computed in `micrOMEGAs`.

The possibility of a multi-component dark sector where a given model constitutes a fraction of the total DM density is a strong one. To address this possibility, we define a relic-abundance parameter

$$f_{\text{rel}} \equiv \frac{\Omega_X}{\Omega_{\text{DM}}}, \quad (19)$$

⁴ `LanHEP` homepage: <http://theory.sinp.msu.ru/~semenov/lanhep.html>.

⁵ `micrOMEGAs` homepage: <https://lapth.cnrs.fr/micromegas/>.

⁶ Brent's method is a root-finding algorithm which combines the bisection method, the secant method and inverse quadratic interpolation.

which quantifies the contribution of X towards the total DM density in our Universe. For plotting purposes, we take $f_{\text{rel}} = 1, 0.1$ and 0.01 corresponding to X relic abundance of 100%, 10% and 1% respectively.

At DM masses below $m_h/2$, we found multiple values of the coupling λ_{hX} at fixed DM masses that were consistent with the Planck measured value. Naively, one expects a monotonic decrease in $\Omega_X h^2$ at larger values of λ_{hX} due to an increased $\langle\sigma v_{\text{rel}}\rangle$, as evident in Eq. (17). However, $\langle\sigma v_{\text{rel}}\rangle$ has an additional dependence on λ_{hX} through the full Higgs boson width $\Gamma_h(\sqrt{s})$ as a function of the centre-of-mass energy \sqrt{s} . Therefore, as λ_{hX} increases, the increasing Higgs boson width counteracts the increase in $\langle\sigma v_{\text{rel}}\rangle$ from λ_{hX} alone and at some point outstrips it, such that $\langle\sigma v_{\text{rel}}\rangle$ starts decreasing with increasing λ_{hX} , causing a minimum relic density $\Omega_X h^2$ for any given DM mass. When these features appear, we always found that only one root was consistent with the Higgs invisible width constraint and this is the one presented in our results. Indeed, the same feature was also seen in the preparation of Ref. [39], but was not explicitly discussed in the final manuscript.

Furthermore, roots of Eq. (18) for $f_{\text{rel}} = 0.1, 0.01$ and DM masses below $m_h/2$ do not exist as the minimum relic density at these masses is larger than the value of the contour being drawn. Consequently, gaps in our relic density contours for $f_{\text{rel}} = 0.1, 0.01$ will appear in our plots.

For masses above $m_h/2$, the relic density monotonically decreases with larger couplings λ_{hX} . This results in a single root (or coupling) at each DM mass that gives the Planck measured relic density. The Higgs invisible width $\Gamma_{\text{inv}}(h \rightarrow \bar{X}X)$ vanishes in this region due to the decay $h \rightarrow \bar{X}X$ becoming kinematically forbidden.

B. Higgs Invisible width

When $m_X < m_h/2$, the decay $h \rightarrow X\bar{X}$ is kinematically allowed. This contributes to the invisible width Γ_{inv} of the SM Higgs boson. The LHC constraints on Γ_{inv} continue to improve as precise measurements of the properties of the Higgs boson are shown to be increasingly in agreement with the SM expectations.

An upper limit of 19% on the SM Higgs invisible branching ratio $\mathcal{BR}(h \rightarrow \bar{X}X)$ at 2σ CL is obtained in Ref. [67] through combined fits to all Higgs production and decay channels probed by ATLAS, CMS and the Tevatron.⁷ An additional projected limit of 5% on the invisible Higgs

⁷ The Higgs invisible branching ratio is defined as $\mathcal{BR}(h \rightarrow X\bar{X}) \equiv \Gamma_{\text{inv}}/(\Gamma_{\text{vis}} + \Gamma_{\text{inv}})$ where $\Gamma_{\text{vis}} \equiv \Gamma_{\text{SM}}$ is the visible contribution of the SM Higgs width.

branching ratio at no more than 1σ CL can be further imposed if no additional Higgs decay is detected at the 14 TeV LHC run after 300 fb^{-1} of luminosity data is collected [68].

For our Higgs-portal models, the Higgs invisible widths are given by [9, 47]

$$\Gamma_{\text{inv}}(h \rightarrow SS) = \frac{\lambda_{hS}^2 v_0^2}{32\pi m_h} \left(1 - \frac{4m_S^2}{m_h^2}\right)^{1/2}, \quad (20)$$

$$\Gamma_{\text{inv}}(h \rightarrow VV) = \frac{\lambda_{hV}^2 v_0^2 m_h^3}{128\pi m_V^4} \left(1 - \frac{4m_V^2}{m_h^2} + \frac{12m_V^4}{m_h^4}\right) \left(1 - \frac{4m_V^2}{m_h^2}\right)^{1/2}, \quad (21)$$

$$\Gamma_{\text{inv}}(h \rightarrow \bar{\chi}\chi) = \frac{m_h v_0^2}{16\pi} \left(\frac{\lambda_{h\chi}}{\Lambda_\chi}\right)^2 \left(1 - \frac{4m_\chi^2}{m_h^2}\right)^{1/2} \left(1 - \frac{4m_\chi^2 \cos^2 \xi}{m_h^2}\right), \quad (22)$$

$$\Gamma_{\text{inv}}(h \rightarrow \bar{\psi}\psi) = \frac{m_h v_0^2}{8\pi} \left(\frac{\lambda_{h\psi}}{\Lambda_\psi}\right)^2 \left(1 - \frac{4m_\psi^2}{m_h^2}\right)^{1/2} \left(1 - \frac{4m_\psi^2 \cos^2 \xi}{m_h^2}\right). \quad (23)$$

Using an upper limit of Y ($Y = 0.19$ or 0.05 from above) on $\mathcal{BR}(h \rightarrow \bar{X}X)$, the Higgs invisible width Γ_{inv} can be expressed in terms of its visible contribution Γ_{vis} through

$$\Gamma_{\text{inv}} \leq \frac{Y}{1-Y} \Gamma_{\text{vis}}. \quad (24)$$

Using the Higgs invisible width expressions from Eqs. (20) to (23), an upper limit on Γ_{inv} in Eq. (24) provides an upper limit on the SM Higgs-DM coupling as a function of the DM mass

$$\begin{aligned} \text{Scalar: } \lambda_{hS} &\leq \left[\frac{Y}{1-Y} \frac{32\pi m_h \Gamma_{\text{vis}}}{v_0^2} \left(1 - \frac{4m_S^2}{m_h^2}\right)^{-1/2} \right]^{1/2}, \\ \text{Vector: } \lambda_{hV} &\leq \left[\frac{Y}{1-Y} \frac{128\pi m_V^4 \Gamma_{\text{vis}}}{v_0^2 m_h^3} \left(1 - \frac{4m_V^2}{m_h^2} + \frac{12m_V^4}{m_h^4}\right)^{-1} \left(1 - \frac{4m_V^2}{m_h^2}\right)^{-1/2} \right]^{1/2}, \\ \text{Majorana: } \frac{\lambda_{h\chi}}{\Lambda_\chi} &\leq \left[\frac{Y}{1-Y} \frac{16\pi \Gamma_{\text{vis}}}{m_h v_0^2} \left(1 - \frac{4m_\chi^2}{m_h^2}\right)^{-1/2} \left(1 - \frac{4m_\chi^2 \cos^2 \xi}{m_h^2}\right)^{-1} \right]^{1/2}, \\ \text{Dirac: } \frac{\lambda_{h\psi}}{\Lambda_\psi} &\leq \left[\frac{Y}{1-Y} \frac{16\pi \Gamma_{\text{vis}}}{m_h v_0^2} \left(1 - \frac{4m_\psi^2}{m_h^2}\right)^{-1/2} \left(1 - \frac{4m_\psi^2 \cos^2 \xi}{m_h^2}\right)^{-1} \right]^{1/2}, \end{aligned}$$

where we take the visible contribution $\Gamma_{\text{vis}} \equiv \Gamma_{\text{SM}} = 4.07 \text{ MeV}$ for $m_h = 125 \text{ GeV}$ [69].

C. Indirect Detection

Indirect detection of DM involve searches for fluxes of γ -rays, e^\pm , p^\pm and neutrinos produced from DM annihilations in distant astrophysical sources. As the annihilation flux (Φ_{ann}) scales as the *square* of the DM mass density (i.e., $\Phi_{\text{ann}} \propto \rho_{\text{DM}}^2$), natural places to look for DM annihilations are those with high DM content such as the dwarf spheroidal (dSph) galaxies, the Galactic Centre

(GC) or our Sun. Current indirect experiments searching for signs of DM annihilations include the Fermi Large Area Telescope (Fermi-LAT) [70], H.E.S.S. [71] and AMS-02 [72]. The upcoming Cherenkov Telescope Array (CTA) [73] is one of the next generation of ground-based gamma-ray telescopes.

To impose parameter space constraints from indirect search experiments, we use a combined log-likelihood function that depends on the model parameters

$$\ln \mathcal{L}_{\text{total}}(m_X, \lambda_{hX}) = \ln \mathcal{L}_{\text{CMB}}(m_X, \lambda_{hX}) + \ln \mathcal{L}_{\text{dSphs}}(m_X, \lambda_{hX}) + \ln \mathcal{L}_{\text{CTA}}(m_X, \lambda_{hX}). \quad (25)$$

In general, the contribution to the total log-likelihood function in Eq. (25) comes from all three indirect searches. However, the CTA log-likelihood function enters in our calculation only when we discuss *projected* limits. Each log-likelihood function depends on m_X and on the Higgs-DM coupling λ_{hX} via the zero-velocity annihilation cross-section⁸ $\langle \sigma v_{\text{rel}} \rangle_0$, the branching ratio \mathcal{B}_f into the SM final state f and the model relic density $\Omega_X h^2$. The final states included in our calculations involve DM annihilations into W^+W^- , ZZ , hh , $\mu^+\mu^-$, $\tau^+\tau^-$ and $q\bar{q}$ for $q = b, c, t$.

We scale all indirect detection signals for each combination of m_X and λ_{hX} by $f_{\text{rel}}^2 = (\Omega_X/\Omega_{\text{DM}})^2$, thereby suppressing signals where X constitutes only a fraction of the total dark matter. In regions where the model relic density is *larger* than the observed DM relic density, we simply rescale in the same way, thereby increasing the expected signals. This is done for the sake of simplicity and is of no practical consequence given that the relevant region is robustly excluded by the relic density constraints.

In complete analogue with the implementation of the relic density constraints, we perform scans in each model parameter space using Brent's method to impose the indirect search limits. The function used for the root-finding algorithm is

$$f_{\text{ID}}(m_X, \lambda_X) = \Delta \ln \mathcal{L}_{\text{total}}(m_X, \lambda_{hX}) - \Delta \ln \mathcal{L}_{\text{CL}}(m_X, \lambda_{hX}), \quad (26)$$

where $\Delta \ln \mathcal{L}_{\text{total}}$ is the combined delta log-likelihood, defined such that it is zero for the case of no DM-signal. The term $\Delta \ln \mathcal{L}_{\text{CL}}$ is the delta log-likelihood for a given confidence level (CL). For our purposes, we implement 1σ and 90% CL limits by taking

$$\Delta \ln \mathcal{L}_{\text{CL}} = \begin{cases} -0.500000 & \text{for } 1\sigma \text{ CL,} \\ -1.352771 & \text{for } 90\% \text{ CL.} \end{cases}$$

⁸ Dark matter annihilations are assumed to occur in the non-relativistic limit since the particles involved have speeds $v \sim 10^{-3}c$. In the zero-velocity limit, the centre-of-mass energy $\sqrt{s} \rightarrow 2m_X$.

When implementing *current* indirect search limits, the combined log-likelihood function is

$$\ln \mathcal{L}_{\text{total}}(m_X, \lambda_{hX}) = \ln \mathcal{L}_{\text{WMAP}}(m_X, \lambda_{hX}) + \ln \mathcal{L}_{\text{dSphs}}(m_X, \lambda_{hX}), \quad (27)$$

whereas for the *projected* future limits, the combined log-likelihood function is

$$\ln \mathcal{L}_{\text{total}}(m_X, \lambda_{hX}) = \ln \mathcal{L}_{\text{Planck}}(m_X, \lambda_{hX}) + \ln \mathcal{L}_{\text{dSphs}}^{\text{projected}}(m_X, \lambda_{hX}) + \ln \mathcal{L}_{\text{CTA}}(m_X, \lambda_{hX}). \quad (28)$$

Here $\ln \mathcal{L}_{\text{dSphs}}^{\text{projected}}(m_X, \lambda_{hX})$ differs from $\ln \mathcal{L}_{\text{dSphs}}(m_X, \lambda_{hX})$ due to the projected improvements of Fermi-LAT in adding more dwarf galaxies to its search, and observing for a longer duration.

When $m_X < m_h/2$, we again encounter situations where multiple values of λ_{hX} satisfy Eq. (26). When this occurs, we ignore the root at larger λ_{hX} and choose the smaller coupling λ_{hX} due to the fact that larger couplings will be robustly excluded by the Higgs invisible width constraints.

1. CMB Likelihood

It is well-known that the temperature fluctuations and polarization of the CMB are sensitive to the redshift of recombination $z \sim 1100$ as it determines the surface of last scattering. If the decay or annihilation of dark matter deposits extra electromagnetic radiation after $z \sim 1100$, it can delay the time taken for recombination and/or produce distortions in the CMB.

A key quantity of interest in determining the CMB bounds on dark matter annihilations is the efficiency $f(z)$ for producing ionising radiation as a function of red-shift z . For annihilations, $f(z)$ is determined in terms of the electromagnetic power injected per unit volume [74]

$$\frac{dE}{dt dV} = f(z) \frac{\langle \sigma v_{\text{rel}} \rangle}{m_X} \Omega_X^2 \rho_{\odot}^2 c^2 (1+z)^6, \quad (29)$$

where $\Omega_X = \rho_X / \rho_c$ and ρ_{\odot} is the local DM mass density.

Bounds on $\langle \sigma v_{\text{rel}} \rangle$ can be encoded in terms of an integral involving $f(z)$ and a set of *principle component* basis functions $e_i(z)$ [75, 76]. In terms of these basis functions, $f(z)$ can be expanded as

$$\varepsilon f(z) = \sum_{i=1}^{\infty} \varepsilon_i e_i(z)$$

where $\varepsilon \equiv \langle \sigma v_{\text{rel}} \rangle / m_X$ and $\varepsilon_i = \varepsilon f(z) \cdot e_i(z) / e_i(z) \cdot e_i(z)$. The inner product is an integral over z with the integration limits $z_1 = 86.83$ and $z_2 = 1258.2$. For annihilating DM, these basis functions are chosen to maximize sensitivity to a generally expected z -dependence of the energy injection from annihilating dark matter in such a way that most important contributions are described by the lowest components.

It is useful to consider the quantity f_{eff} defined in terms of a “universal WIMP annihilation curve” $e_W(z)$ as $f_{\text{eff}} \sim (f \cdot e_W)/(e_W \cdot e_W)$, which has the interpretation that $f_{\text{eff}} < 1$ denotes the average efficiency of energy injection for the annihilation channel under consideration. With the expansion $e_W = \sum_i c_i e_i$ for WMAP7 [77], only the first principle component is dominant. Hence, f_{eff} for WMAP7 is given by

$$f_{\text{eff}} \equiv \frac{(f \cdot e_1)}{c_1(e_1 \cdot e_1)} \quad (\text{WMAP})$$

where numerically $c_1 = 4.64$. For Planck [61], the contribution from all three principle components must be included and therefore

$$f_{\text{eff}} \equiv \frac{1}{\sqrt{\lambda_1} c_1} \left[\lambda_i \left(\frac{f \cdot e_i}{e_i \cdot e_i} \right)^2 \right]^{1/2} \quad (\text{Planck})$$

where λ_i and e_i are parameters appropriate for Planck.

We use the tabulated values of the effective efficiency (f_{eff}) for various SM final states and DM masses from Ref. [74]. At intermediate masses, we interpolate the values of f_{eff} in terms of $\log_{10} m_X$. For DM annihilation into multiple channels, the total f_{eff} is a weighted sum of effective efficiency $f_{\text{eff},f}$ over final states f with branching ratio \mathcal{B}_f as

$$f_{\text{eff}} = \sum_f \mathcal{B}_f f_{\text{eff},f}. \quad (30)$$

To impose CMB constraints at arbitrary CL, we use a log-likelihood function for the annihilation cross-section $\langle \sigma v_{\text{rel}} \rangle$, assuming a DM mass m_X and a branching ratio \mathcal{B}_f into final state f . For the Planck experiment, the log-likelihood is given by [74]

$$\ln \mathcal{L}_{\text{Planck}}(\langle \sigma v_{\text{rel}} \rangle | m_X, \mathcal{B}_f) = -\frac{1}{2} f_{\text{eff}}^2 \lambda_1 c_1^2 \left(\frac{\langle \sigma v_{\text{rel}} \rangle}{2 \times 10^{-27} \text{cm}^3 \text{s}^{-1}} \right)^2 \left(\frac{\text{GeV}}{m_X} \right)^2, \quad (31)$$

where $c_1 = 4.64$ and $\lambda_1 = 3.16$.⁹ The above equation assumes a linear response on the CMB against the deposited energy, which is not accurate for WMAP. This however can be corrected by the replacement $2 \times 10^{-27} \text{cm}^3 \text{s}^{-1} \rightarrow 3.2 \times 10^{-27} \text{cm}^3 \text{s}^{-1}$ and $\lambda_1 = 0.279$. Therefore, for the WMAP experiment, the log-likelihood is given by [74]

$$\ln \mathcal{L}_{\text{WMAP}}(\langle \sigma v_{\text{rel}} \rangle | m_X, \mathcal{B}_f) = -\frac{1}{2} f_{\text{eff}}^2 \lambda_1 c_1^2 \left(\frac{\langle \sigma v_{\text{rel}} \rangle}{3.2 \times 10^{-27} \text{cm}^3 \text{s}^{-1}} \right)^2 \left(\frac{\text{GeV}}{m_X} \right)^2, \quad (32)$$

where $c_1 = 4.64$ and $\lambda_1 = 0.279$.

⁹ This is in fact a projected log-likelihood for the Planck polarization data, but it agrees very well with the actual constraints in Ref. [78].

2. Fermi dwarfs Likelihood

To place upper limits on $\langle\sigma v_{\text{rel}}\rangle$, one must quantify how it influences the flux of gamma-rays detected by the Large Area Telescope aboard the Fermi satellite (Fermi-LAT) [79]. The non-observation of gamma-rays from the dwarf spheroidal satellite galaxies of the Milky Way (dSphs) can be used to place strong upper limits on $\langle\sigma v_{\text{rel}}\rangle$ in various SM final states.

The differential gamma-ray flux from DM annihilation in a region $\Delta\Omega$ towards a dwarf spheroidal galaxy is given by

$$\frac{d\Phi_{\text{ann}}}{dE} = \underbrace{\frac{\langle\sigma v_{\text{rel}}\rangle}{8\pi m_X^2} \frac{dN_\gamma}{dE}}_{\Phi_{\text{PP}}} \underbrace{\int_{\Delta\Omega} d\Omega \int_{\text{l.o.s}} \rho_{\text{DM}}^2(r) dl}_{J_{\text{ann}}}. \quad (33)$$

The first term Φ_{PP} describes the particle physics aspect of DM annihilation: the velocity-averaged annihilation cross-section $\langle\sigma v_{\text{rel}}\rangle$, the differential gamma-ray spectrum dN_γ/dE per annihilation¹⁰ and the dark matter mass m_X . The second term J_{ann} is commonly known as the ‘ J factor’, and describes the astrophysical aspects of a dwarf galaxy. It is determined by an integral over the line-of-sight (l) and solid angle of the DM density profile $\rho_{\text{DM}}(r)$ where $r \equiv r(l, \psi) = \sqrt{r_\odot^2 + l^2 - 2lr_\odot \cos\psi}$ is the distance from the GC and r_\odot is the distance between our Sun and the GC.

The main advantage of the form of the differential gamma-ray flux in Eq. (33) is that the terms describing the particle physics of DM annihilation (specifically Φ_{PP}) and the astrophysics of a dwarf galaxy (specifically J_{ann}) separate into two independent factors. Since the pre-factor Φ_{PP} is constant for a given set of model parameters, only the J factors have to be determined individually for each dwarf galaxy. A combined analysis based on the observations of multiple dwarf satellite galaxies is therefore straightforward.

The expected number of gamma-rays produced from DM annihilations between energies E_1 and E_2 in a specific region of the sky is

$$N_{\text{ann}} = T_{\text{obs}} \frac{\langle\sigma v_{\text{rel}}\rangle J_{\text{ann}}}{8\pi m_X^2} \int_{E_1}^{E_2} dE \frac{dN_\gamma}{dE} A_{\text{eff}}(E) \phi(E), \quad (34)$$

where T_{obs} is the experimental observation time, $A_{\text{eff}}(E)$ is the energy-dependent effective area and $\phi(E)$ is the detector energy resolution.

The Fermi-LAT is a powerful tool in searching for signs of DM annihilations from distant astrophysical sources. Currently, it provides the strongest upper bounds on $\langle\sigma v_{\text{rel}}\rangle$, based on a

¹⁰ Specifically, the differential gamma-ray spectrum per annihilation is a sum over the differential spectrum from all possible final states: $dN_\gamma/dE = \sum_f \mathcal{B}_f dN_\gamma^f/dE$, where \mathcal{B}_f is the branching ratio into the SM final state f .

combined analysis of 15 dwarf spheroidal galaxies in the Milky Way using 6 years of Fermi-LAT data, processed with the new **Pass-8** event-level analysis [80].¹¹ For each of the 15 dwarf galaxies included in the analysis, the results are publicly available in the form of tabulated values of the energy times integrated gamma-ray flux (i.e., $E\Phi_{\text{ann}}$ in units of $\text{MeV cm}^{-2} \text{s}^{-1}$) and delta log-likelihoods ($\Delta \ln \mathcal{L}_{\text{dSphs}}$) in 24 energy bins between 500 MeV and 500 GeV.

In our analysis, we calculate the Fermi dwarfs log-likelihood ($\ln \mathcal{L}_{\text{dSphs}}$) using **gamLike**,¹² a package aimed at the evaluation of log-likelihoods from gamma-ray searches for DM. It is primarily written in **C++** and comes with various routines which integrate the input arrays of $\Phi_{\text{PP}}(E)$ in each of the energy bins relevant for a given experiment. The integrated $\Phi_{\text{PP}}(E)$ are combined with the J factors, giving an array of integrated gamma-ray fluxes (Φ_{ann}) in each energy bin. The integrated flux times energy ($E\Phi_{\text{ann}}$) arrays are compared with the tabulated log-likelihood values. Finally, a log-likelihood value at a fixed set of model parameters is returned by summing over the interpolated log-likelihood values in each energy bin.

The inputs to the **gamLike** package are arrays of gamma-ray energies E (GeV) and $\Phi_{\text{PP}}(E)$ ($\text{cm}^3 \text{s}^{-1} \text{GeV}^{-3}$) where

$$\Phi_{\text{PP}}(E) = \frac{\langle \sigma v_{\text{rel}} \rangle}{8\pi m_X^2} \frac{dN_\gamma(E)}{dE}. \quad (35)$$

Since the tabulated results of Ref. [80] are given between gamma-ray energies of 500 MeV and 500 GeV, we interpolate the differential gamma-ray spectrum dN_γ/dE calculated within **micrOMEGAs** between 500 MeV and the DM mass m_X .¹³ The $\ln \mathcal{L}_{\text{dSphs}}(m_X, \lambda_{hX})$ entering in Eq. (27) is then a difference of the log-likelihoods for a DM-signal and background-only hypothesis (i.e., $\Phi_{\text{PP}} = 0$).

For *projected* indirect search limits, we assume that Fermi operates for at least 10 years in its current survey mode and is able to add as many southern dwarf galaxies in the future as there are mostly northern dwarf galaxies now. Assuming that the limits on $\langle \sigma v_{\text{rel}} \rangle$ scale with \sqrt{N} , following an improvement in the signal-to-noise ratio, we calculate the projected Fermi sensitivities by scaling the current limits by a factor of $\sqrt{2 \times 10/6} = \sqrt{20/6} \sim 1.83$.

3. CTA Likelihood

The Cherenkov Telescope Array (CTA) is a multi-national project to build the next generation of ground-based gamma-ray instruments and to have sensitivity over energies from a few tens of

¹¹ https://www-glast.stanford.edu/pub_data/1048/.

¹² C. Weniger et al., to be released soon.

¹³ The differential gamma-ray spectrum dN_γ/dE is zero after $E = m_X$.

GeV to 100 TeV. It is intended to improve the flux sensitivities of the current generation of Imaging Atmospheric Cherenkov Telescopes (IACTs) such as MAGIC [81], H.E.S.S. [82] and VERITAS [83] by an order of magnitude.

CTA will consist of several tens of telescopes of 2–3 different types, with size varying between 5 and 25 metres, distributed over an area of several square kilometres. The sensitivity will be a factor of 10 better than current instruments, and the Field of View (FoV) will be up to 10° in diameter. It is envisaged as a two part telescope, with southern and northern sites. CTA South is most relevant for DM searches towards the GC. Its final design is not yet fixed. Apart from the construction and maintenance questions, the relevant remaining design choices are the relative emphasis on the higher or lower energies, the angular and energy resolution and the FoV. A first detailed Monte Carlo (MC) analysis was presented in Ref. [84] where 11 different array configurations for the CTA South were discussed.

We use the array configuration known as ‘Array I’, which has a balanced configuration with 3 large (~ 24 m aperture), 18 medium (~ 12 m) and 56 small-sized telescopes (~ 4 –7 m). This configuration also provides a good compromise in sensitivity between lower and higher energies. Extensive information on the effective area, background rates, angular and energy resolution of Array I is also available. Furthermore, previous DM sensitivity studies have used a very similar array: Array E in Ref. [85] and the Paris-MVA analysis of Array I in Ref. [86]. The point-source sensitivities of Arrays E and I agree very well at energies $\lesssim 1$ TeV, whereas at higher energies Array I is more sensitive (only by a factor of less than two).

The main performance aspects of Array I include an effective area of 100 m^2 at its threshold energy of 20 GeV, which then increases quickly to about $4 \times 10^5 \text{ m}^2$ at 1 TeV and $3 \times 10^6 \text{ m}^2$ at 10 TeV. The angular resolution in terms of the 68% containment radius is about $r_{68} \simeq 0.3^\circ$ at threshold and drops to below 0.06° at energies above 1 TeV. The energy resolution is relatively large at threshold, $\sigma(E)/E \sim 50\%$, but drops to below 10% at energies above 1 TeV.

Following the analysis of Ref. [87], we use their tabulated values of the integrated gamma-ray flux times energy (i.e., $\Phi_{\text{ann}} E$ in units of $\text{MeV cm}^{-2} \text{ s}^{-1}$) and log-likelihoods ($\ln \mathcal{L}_{\text{CTA}}$) between gamma-ray energies of 25 GeV and 10 TeV. The main features of their study are:

- Assessing the impacts of all backgrounds, including protons and electrons in cosmic rays hitting the atmosphere and diffuse astrophysical emissions. Galactic diffuse emission (GDE) substantially degrades the CTA differential sensitivity (see Fig. 4 of Ref. [87] for a comparison).

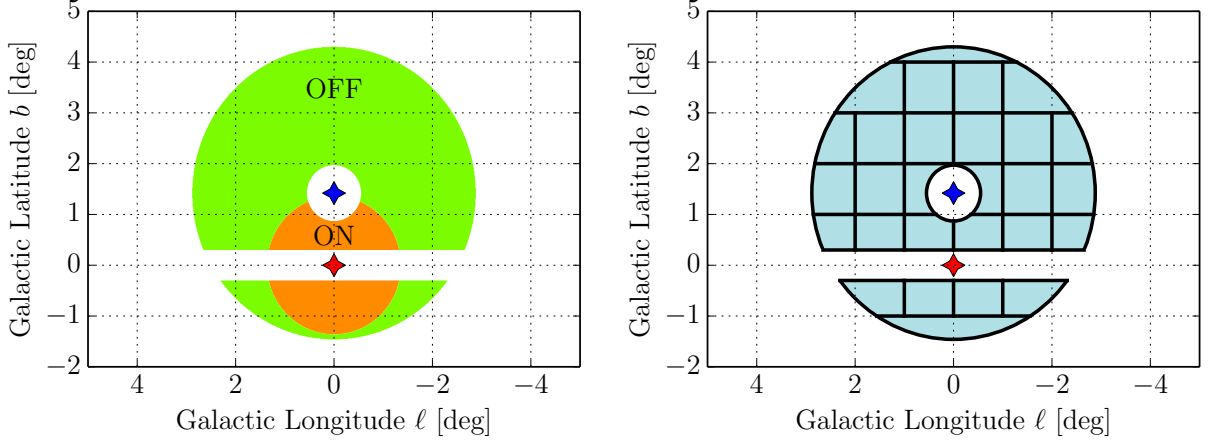


FIG. 1: Figures adopted with permission from Ref. [87]. *Left:* The ‘signal’ and ‘background’ Region of Interests (RoIs) used in the Ring method of Ref. [88]. *Right:* Separation of the ‘signal’ and ‘background’ RoIs into 28 sub-RoIs for the morphological analysis of Ref. [87].

- Introducing a statistical framework that accounts for the impacts of differential acceptance uncertainties from sources such as event reconstruction, Monte Carlo (MC) determination of the effective areas and the uncertainty in atmospheric conditions [89] within a FoV on DM limits from CTA. Specifically, the tabulated results correspond to a systematic uncertainty of 1%.
- Using the Einasto profile [90] to calculate the J factors for the GC. The Einasto profile best fits the DM density profiles seen in the N -body simulations of Milky Way type galaxies

$$\rho_{\text{DM}}(r) \propto \exp \left(-\frac{2}{\alpha} \left[\left(\frac{r}{r_s} \right)^\alpha - 1 \right] \right), \quad (36)$$

where the profile is normalised to a local DM density of $\rho_{\text{DM}}(r_\odot) = 0.4 \text{ GeV cm}^{-3}$ by choosing $\alpha = 0.17$, $r_s = 20 \text{ kpc}$ and $r_\odot = 8.5 \text{ kpc}$ [91].

- Using a slightly contracted generalised NFW profile [92] to indicate how the limits improve with a more optimistic DM distribution. The profile is parametrised as

$$\rho_{\text{DM}}(r) \propto \frac{1}{r^\gamma (r_s + r)^{3-\gamma}}, \quad (37)$$

where $\gamma = 1.3$ is the inner slope of the profile and $r_s = 20 \text{ kpc}$ is the scale radius. It is normalised in the same way as the Einasto profile (i.e., $\rho_{\text{DM}}(r_\odot) = 0.4 \text{ GeV cm}^{-3}$).

- Performing a ‘morphological’ analysis by covering the area occupied by the two RoIs in the left panel of Fig. 1 and dividing it into $1^\circ \times 1^\circ$ squares, giving a total of 28 RoIs as shown

in the right panel of Fig. 1. The morphological analysis allows for a proper exploitation of the shape differences between the GDE, which is concentrated along the Galactic plane, and the DM annihilation signal, which is spherically distributed around the GC. The resultant constraints are found to be more stringent by a factor of a few when compared against traditional “Ring” analyses.

In summary, the tabulated results of Ref. [87] are based on a morphological analysis over the 28 RoIs, assuming $\gtrsim 100$ hrs of GC observation by CTA,¹⁴ 1% instrumental systematics, J factors for the GC using the Einasto profile (Eq. 36) and inclusion of all known backgrounds (cosmic ray electrons/protons, and the galactic diffusion emissions).

In analogy with the Fermi dwarfs log-likelihood calculation, we use the `gamLike` package to calculate the CTA log-likelihood from the tabulated results of Ref. [87]. As these results are for gamma-ray energies between 25 GeV and 10 TeV, the corresponding input parameters to the `gamLike` package are arrays of gamma-ray energies E (GeV) (between 25 GeV and m_X) and $\Phi_{\text{PP}}(E)$ ($\text{cm}^3 \text{s}^{-1} \text{GeV}^{-3}$).

Limits on $\langle\sigma v_{\text{rel}}\rangle$ from CTA observation of the GC are presented in Fig. 7 of Ref. [87] where different annihilation channels and DM halo profiles are assumed. For the DM annihilation into $b\bar{b}$ final state, a contracted generalised NFW profile (Eq. 37) yields a factor of 6 better limits on $\langle\sigma v_{\text{rel}}\rangle$ when compared against the Einasto profile (Eq. 36). This is mainly due to an increase in the GC J factors by a factor of 2.9 (when summed over all RoIs). To extend the expected search capability of CTA towards higher WIMP masses, we apply these improved limits in order to see the effect of using a more optimistic DM distribution.

D. Direct Detection

Direct detection experiments aim to measure the recoil of a nucleus in a collision with a DM particle. After an elastic collision between DM of mass m_X and a nucleus of mass M , the nucleus recoils with energy $E = \mu^2 v^2 (1 - \cos \theta)/M$, where $\mu \equiv m_X M/(m_X + M)$ is the DM-nucleus reduced mass, v is the speed of DM particle relative to the nucleus rest frame and θ is the scattering angle in the centre-of-mass (COM) frame.

The differential rate per day (given in units of $\text{cpd kg}^{-1} \text{keV}^{-1}$ where cpd is counts per day)

¹⁴ Since the limits of Ref. [87] are systematics dominated, they are more or less independent of any increase in the CTA observation time beyond 100 hrs. For our portal models, we derive the indirect search limits based on 100 hrs of CTA observation time.

from primarily spin-independent (SI) interactions is given by [93, 94]

$$\frac{dR}{dE} = \frac{\rho_\odot}{m_X M} \int dv v f(v, t) \frac{d\sigma_X^{\text{SI}}}{dE}, \quad (38)$$

where ρ_\odot is local DM mass density and $f(v, t)$ is the time-dependent DM velocity distribution. The term $d\sigma_X^{\text{SI}}/dE$ is the momentum-dependent differential SI cross-section. In the typical case where the target material contains more than one isotope, the differential rate is given by a mass-fraction weighted sum over contributions from the isotopes, each of the form given by Eq. (38).

The momentum-dependent differential SI cross-section is given by

$$\frac{d\sigma_X^{\text{SI}}}{dE} = \frac{1}{E_{\text{max}}} \sigma_0 F^2(q) \Theta(q_{\text{max}} - q), \quad (39)$$

where $E_{\text{max}} = q_{\text{max}}^2/2M = 2\mu^2 v^2/M$ is the maximum energy transfer in a collision at a relative velocity v , σ_0 is the SI cross-section in the zero-velocity limit¹⁵ and Θ is the Heaviside step-function. The term $F(q)$ is the form-factor accounting for the finite-size of the nucleus. When DM coherently scatters off the entire nucleus with low momentum transfer, $F^2(q) \rightarrow 1$. However, when the de Broglie wavelength of the momentum transfer q becomes comparable to the size of the nucleus, DM becomes sensitive to the internal structure of the nucleus and $F^2(q) < 1$, with $F^2(q) \ll 1$ at high momentum transfers.

It is traditional to define an *effective* SI cross-section corrected with the form-factor as

$$\sigma(q) \equiv \sigma_0 F^2(q), \quad (40)$$

such that the dependency on the momentum transfer q is contained entirely within the form-factor $F^2(q)$. The *actual* cross-section is $\int dq^2 d\sigma_X^{\text{SI}}(q^2, v)/dq^2$ for a given DM-nucleus relative speed v . With the chosen convention in Eq. (40), the expression for the momentum-dependent differential SI cross-section in Eq. (39) simplifies to

$$\frac{d\sigma_X^{\text{SI}}}{dE} = \frac{M}{2\mu^2 v^2} \sigma(q) \Theta(q_{\text{max}} - q). \quad (41)$$

With the form of the the momentum-dependent differential SI cross-section in Eq. (41), the differential rate per day in Eq. (38) becomes

$$\frac{dR}{dE} = \frac{1}{2m_X \mu^2} \sigma(q) \rho_\odot \eta(v_{\text{min}}(E), t), \quad (42)$$

¹⁵ Generally, σ_{SI} and σ_{SD} are used to represent this term for nuclear spin-independent (SI) and spin-dependent (SD) interactions respectively. To avoid confusion with existing literatures, we will represent the SI contribution to σ_0 as σ_{SI} in our models.

where

$$\eta(v_{\min}, t) = \int_{v > v_{\min}} d^3v \frac{f(v, t)}{v} \quad (43)$$

is the mean inverse speed and

$$v_{\min}(E) = \sqrt{\frac{ME}{2\mu^2}}$$

is the minimum DM speed that results in a nucleus recoil with energy E . The requirement $q < q_{\max}$ in the Heaviside step-function of Eq. (41) results in a lower limit $v > v_{\min}$ on the integral in Eq. (43).

The main advantage of writing the recoil spectrum in the form of Eq. (42) instead of Eq. (38) is that the particle physics and astrophysics aspects separate into two distinct factors: $\sigma(q)$ describes the particle physics aspect; while ρ_{\odot} and $\eta(v_{\min}, t)$ describe the astrophysical aspect.

For our Higgs-mediated scalar and/or pseudoscalar DM coupling, the SI cross-section (σ_{SI}) takes the form

$$\sigma_{\text{SI}} = \frac{\mu^2}{\pi} \left[Z G_p^{\text{SI}} + (A - Z) G_n^{\text{SI}} \right]^2 + \frac{q^2}{4m_X^2} \frac{\mu^2}{\pi} \left[Z \tilde{G}_p^{\text{SI}} + (A - Z) \tilde{G}_n^{\text{SI}} \right]^2, \quad (44)$$

where Z and $A - Z$ are the number of protons and neutrons in the nucleus respectively and $G_N^{\text{SI}} (\tilde{G}_N^{\text{SI}})$ for $N = p, n$ are the effective scalar (pseudoscalar) DM-nucleon couplings in analogue with the G_F -like effective four-fermion coupling constants [95]. For the scalar and vector models, $\tilde{G}_N^{\text{SI}} = 0$ whereas in fermion models both terms contribute to σ_{SI} . Due to the $q^2/4m_X^2$ factor arising from the pseudoscalar DM-nucleon interaction [96] in fermion models, the corresponding detection rates are momentum suppressed.

When the effective scalar and pseudoscalar couplings are approximately equal for protons and neutrons, leading to $\sigma_{\text{SI},p} \simeq \sigma_{\text{SI},n}$, the SI cross-section in Eq. (44) is enhanced by a factor of A^2 because the matrix elements for the cross-section are a coherent sum over the individual protons and neutrons in the nucleus.

For the SI interaction, the form factor is a Fourier transform of the nucleus mass distribution. As a reasonably accurate approximation, we use the Helm form factor [97], which was first introduced as a modification to the form factor for a uniform sphere with a Gaussian function to account for the soft edge of the nucleus [98]. It is given by

$$F(q) = 3e^{-q^2 s^2/2} \left[\frac{\sin(qr_n) - qr_n \cos(qr_n)}{(qr_n)^3} \right], \quad (45)$$

where $s \simeq 0.9$ fm and $r_n^2 = c^2 + \frac{7}{3}\pi^2 a^2 - 5s^2$ is the effective nuclear radius with $a \simeq 0.52$ fm and $c \simeq 1.23A^{1/3} - 0.60$ fm.

We use the standard astrophysical parameters, namely the local DM density $\rho_\odot = 0.4 \text{ GeV cm}^{-3}$ and the local galactic disk rotation speed $v_{\text{rot}} = 220 \text{ km s}^{-1}$, with the same value for the most probable speed \bar{v} of the Maxwell-Boltzmann velocity distribution. We take the Galactic escape speed as $v_{\text{esc}} = 544 \text{ km s}^{-1}$ (see Ref. [99] for a discussion).

In the standard analysis where only a single component of DM constitutes the total DM relic density, the differential rate of detection is proportional to $(\rho_\odot/m_X)\sigma_{\text{SI}}$ as evident in Eq. (42). To address the multi-component dark matter scenario in our models, we rescale the limiting value of σ_{SI} by the fraction $f_{\text{rel}} = \Omega_X/\Omega_{\text{DM}}$ of the energy density contributed by X to the total DM density. This results in the local X energy density of $f_{\text{rel}} \rho_\odot$.

1. Non-fermion models

The SI cross-section in scalar and vector models are given by

$$\text{Scalar: } \sigma_{\text{SI}} = \frac{\mu^2}{\pi} \frac{\lambda_{hS}^2 f_N^2 m_N^2}{4m_S^2 m_h^4} = \frac{m_N^4}{4\pi(m_S + m_N)^2} \frac{\lambda_{hS}^2 f_N^2}{m_h^4}, \quad (46)$$

$$\text{Vector: } \sigma_{\text{SI}} = \frac{\mu^2}{\pi} \frac{\lambda_{hV}^2 f_N^2 m_N^2}{4m_V^2 m_h^4} = \frac{m_N^4}{4\pi(m_V + m_N)^2} \frac{\lambda_{hV}^2 f_N^2}{m_h^4}, \quad (47)$$

where $m_N = 0.931 \text{ GeV}$ and $f_N = 0.30$ [39] (see also Ref. [100]). The term f_N is related to the quark matrix elements inside nucleons through

$$f_N = \sum_{\text{quarks}} f_{Tq}^{(N)} = \sum_{\text{quarks}} \frac{m_q}{m_N} \langle N | \bar{q}q | N \rangle = \frac{2}{9} + \frac{7}{9} \sum_{q=u,d,s} f_{Tq}^{(N)}, \quad (48)$$

where the last equality follows from the heavy-quark expansion [101].

For the XENON1T [102–104] experiment, we apply the 90% CL limits from XENON100 [105] appropriately weighted by the fraction $f_{\text{rel}} = \Omega_X/\Omega_{\text{DM}}$ of dark matter. Assuming that the sensitivity as a function of DM mass scales relative to that of XENON100 simply by the exposure ε , we demand for every value of $\{m_X, \lambda_{hX} | X \in S, V\}$ that

$$\sigma_{\text{eff}}(m_X, \lambda_X) \equiv \varepsilon f_{\text{rel}} \sigma_{\text{SI}}(m_X, \lambda_X) \leq \sigma_{\text{Xe}} \quad (49)$$

where σ_{Xe} is the 90% CL limit from XENON100. For the projected XENON1T, the expected improvement in sensitivity over XENON100 is $\varepsilon = 100$.

For the LUX [106, 107] experiment, we construct the log-likelihood function from the Poisson distribution [108] in the observed number of signal events N by

$$\mathcal{L}(s|N) = P(N|s) = \frac{(b+s)^N e^{-(b+s)}}{N!}, \quad (50)$$

where b is the expected number of background events and

$$s = MT \int_0^\infty dE \phi(E) \frac{dR}{dE} \quad (51)$$

is the expected number of signal events, MT is the detector mass \times exposure and $\phi(E)$ is a global efficiency factor incorporating trigger efficiencies, energy resolution and analysis cuts.

We perform the LUX log-likelihood calculations using the `LUXCalc` [109] package.¹⁶ For the LUX analysis region, we use $N = 1$ and $b = 0.64$ [110]; while for XENON100, we use $N = 2$ and $b = 1$ [105]. The efficiency curves $\phi(E)$ are generated by TPMC [111] using the NEST [112, 113] model.¹⁷

The `LUXCalc` package requires as inputs the effective SI scalar DM-nucleon coupling G_N^{SI} and the pseudoscalar DM-nucleon coupling \tilde{G}_N^{SI} to calculate the SI cross-section in Eq. (44). For the scalar and vector models, the effective DM-nucleon couplings are

$$\text{Scalar: } G_N^{\text{SI}} = \frac{\lambda_{hS} f_N m_N}{2m_S m_h^2}, \quad \tilde{G}_N^{\text{SI}} = 0, \quad (52)$$

$$\text{Vector: } G_N^{\text{SI}} = \frac{\lambda_{hV} f_N m_N}{2m_V m_h^2}, \quad \tilde{G}_N^{\text{SI}} = 0, \quad (53)$$

which reproduces the SI cross-sections in Eqs. (46) and (47) respectively. The pseudoscalar effective DM-nucleon couplings are zero because the interaction between DM and the nucleons proceeds through a spin 0 gauge boson.

2. Fermion models

Due to the mediator being a spin 0 boson, the interactions between DM and nucleons are nucleon-spin independent. From the Majorana and Dirac model Lagrangians in Eqs. (14) and (15) respectively, a mixing between a pure scalar ($\cos \xi = 1$) and a pure pseudoscalar ($\cos \xi = 0$) interaction occurs.

For a pure pseudoscalar interaction, the SI cross-section is suppressed by a factor of $q^2/4m_X^2$ [96], where q is the momentum transfer. A direct comparison between the analytical SI cross-section expressions and the limits imposed by XENON100 or LUX experiments is not accurate. We therefore use a generalised and augmented version of `LUXCalc` to include the $q^2/4m_X^2$ factor in the differential rate per day dR/dE .

¹⁶ `LUXCalc` homepage: <http://chris.savage.name/LUXCalc/>.

¹⁷ NEST homepage: <http://nest.physics.ucdavis.edu/site/>.

For the Majorana and Dirac fermion models, the effective scalar and pseudoscalar DM-nucleon couplings required by **LUXCalc** are

$$\begin{aligned} \text{Majorana: } G_N^{\text{SI}} &= \frac{\lambda_{h\chi}}{\Lambda_\chi} \frac{f_N m_N \cos \xi}{m_h^2}, & \tilde{G}_N^{\text{SI}} &= \frac{\lambda_{h\chi}}{\Lambda_\chi} \frac{f_N m_N \sin \xi}{m_h^2}, \\ \text{Dirac: } G_N^{\text{SI}} &= \frac{\lambda_{h\psi}}{\Lambda_\psi} \frac{f_N m_N \cos \xi}{m_h^2}, & \tilde{G}_N^{\text{SI}} &= \frac{\lambda_{h\psi}}{\Lambda_\psi} \frac{f_N m_N \sin \xi}{m_h^2}. \end{aligned}$$

For the XENON1T experiment, the expected improvement in sensitivity over XENON100 is $\varepsilon = 100$, whereas for the LUX experiment, limits are derived with $\varepsilon = 1$.

With the inclusion of the momentum-suppressed term in the differential rate per day, we perform root-finding scans in the $(m_X, \lambda_{hX}/\Lambda_X)$ plane for $X \in (\chi, \psi)$ using Brent's method. The function for the root-finding algorithm is

$$f_{\text{DD}}(m_X, \lambda_X) = \Delta \ln \mathcal{L}_{\text{Poisson}}(m_X, \lambda_{hX}) - \Delta \ln \mathcal{L}_{90\% \text{ CL}}(m_X, \lambda_{hX}) \quad (54)$$

where $\Delta \ln \mathcal{L}_{\text{Poisson}}$ is the difference of $\ln \mathcal{L}_{\text{Poisson}}$ (Eq. 50) between a DM signal ($s \neq 0$) and no DM signal ($s = 0$) whereas $\Delta \ln \mathcal{L}_{90\% \text{ CL}} = -1.352771$ is the delta log-likelihood for a 90% CL.

IV. RESULTS

Having outlined an implementation of our model constraints from various experiments, we now present our results. As our current study is a generalisation of the scalar singlet analysis in Ref. [39] to non-scalar models, we first start by presenting our scalar model results obtained using **micrOMEGAs** to validate their consistency.

Although QCD corrections for quark final states at low scalar masses were included in Ref. [39], they are absent in our analysis because their inclusion in either **micrOMEGAs** or **LanHEP** is rather non-trivial, given the fact that **micrOMEGAs** relies heavily on auto-generated **LanHEP** codes.

The relic density from **micrOMEGAs** shows a local step-function reduction of 5–12% in a small range of couplings over the mass range $100 \lesssim m_{S,V}/\text{GeV} \lesssim 400$ and $5 \lesssim m_{\chi,\psi}/\text{TeV} \lesssim 180$. This feature is not reproduced in the annihilation cross-section, nor relic densities from the **micrOMEGAs** routines employing the freeze-out approximation, nor in our previous calculations for the scalar model [39]. Away from the feature, the full **micrOMEGAs** relic densities are in good agreement with the freeze-out approximation and our previous results [39]. The drop appears symptomatic of a numerical error in the full **micrOMEGAs** Boltzmann solver, possibly due to poor convergence properties (it is not solved by the *accurate* setting). As the regions where this occurs are only a few tenths of a unit wide in the log of λ_{hX} , we simply omit them from our limit curves, interpolating across the small resulting gap.

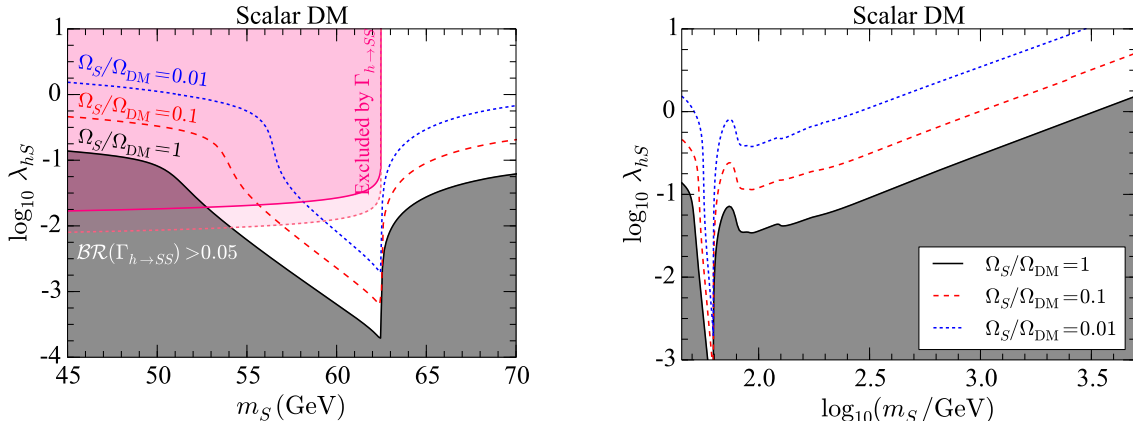


FIG. 2: Contours of fixed scalar relic density for $f_{\text{rel}} = 1$ (black solid), 0.1 (red dashed) and 0.01 (blue dotted). The grey shaded region is excluded due to an overabundance of dark matter. *Left*: A close-up of the resonantly enhanced annihilation region, $m_S \sim m_h/2$. Larger values of λ_{hS} are excluded by an upper limit of 19% (pink solid) at 2σ CL or 5% (pink dotted) at 1σ CL on $\mathcal{BR}(h \rightarrow SS)$. *Right*: Relic density contours for the full range of m_S .

A. Scalar model

We perform scans in the (m_S, λ_{hS}) plane and generate contours of fixed scalar relic density ($\Omega_S h^2$) for $f_{\text{rel}} = 1$ (black solid), 0.1 (red dashed) and 0.01 (blue dotted) as shown in Fig. 2. Values of λ_{hS} in the grey shaded region are excluded by the relic density constraints. This is due to the fact that a lower value of λ_{hS} gives smaller $\langle \sigma v_{\text{rel}} \rangle$. Following Eq. (17), there is therefore an overabundance of the scalar S relic density.

In the region $m_S < m_h/2$, an upper limit of 19% (pink solid) at 2σ CL and 5% (pink dotted) at 1σ CL on the Higgs invisible branching ratio $\mathcal{BR}(h \rightarrow SS)$ excludes coupling larger than $\log_{10} \lambda_{hS} \sim -1.75$ and $\log_{10} \lambda_{hS} \sim -2.1$ respectively. The combined constraints on the scalar relic density and the Higgs invisible width exclude lower scalar masses apart from a small triangle between 54 GeV and $m_h/2$.

Near the resonance $m_S \sim m_h/2$, the annihilation cross-section σv_{rel} is enhanced. Consequently, the relic density contours move to lower values of λ_{hS} to compensate for the enhancement. Above $m_S > m_h/2$, the relic density contours scale essentially linearly with $\log_{10} m_S$.

In Fig. 3, we show the combined sensitivity of indirect searches to various regions of the scalar model parameter space. For the current limits, which include the combined analysis of 15 dwarf galaxies by Fermi-LAT [80] and 7-year observation of the CMB (WMAP7) [77], we only present 1σ CL limits (brown solid). The region $m_h/2 \lesssim m_S < 70$ GeV with $\log_{10} \lambda_{hS} \in [-2.5, -1]$ can be seen

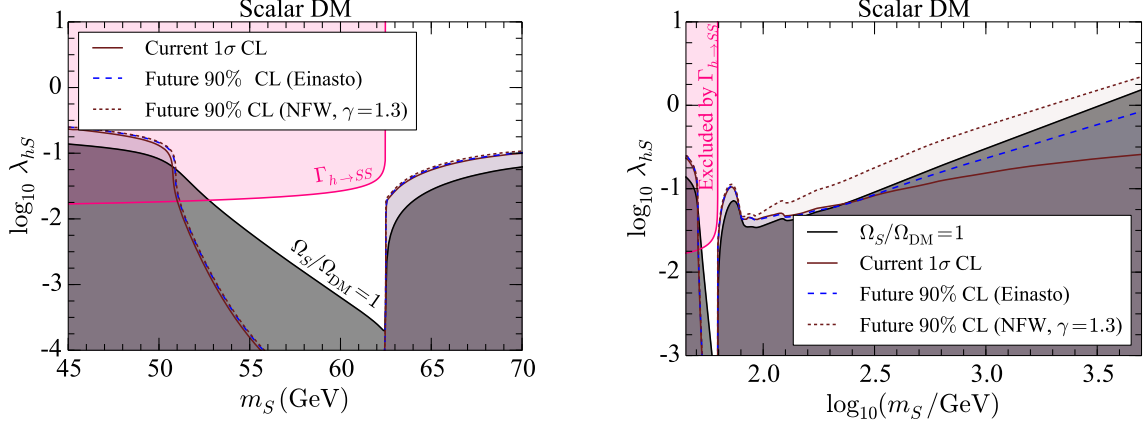


FIG. 3: Indirect search limits on the scalar model parameter space. The grey and pink shaded regions are excluded respectively by the observed DM relic density and an upper limit of 19% on $\mathcal{BR}(h \rightarrow SS)$ at 2σ CL. Values of λ_{hS} below the current 1σ CL (brown solid) curve are excluded at more than 1σ CL. Regions below the future 90% CL curve with the Einasto (blue dashed) and contracted NFW (brown dotted) profiles will be excluded. *Left:* A close-up of the resonant annihilation region, $m_S \sim m_h/2$. *Right:* The full range of m_S .

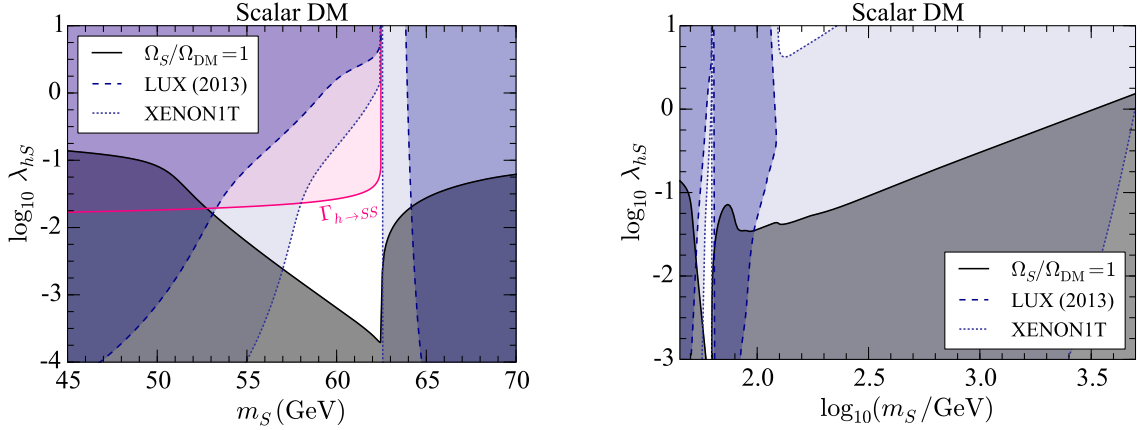


FIG. 4: Direct search limits on the scalar model parameter space. The grey shaded regions are ruled out by the observed relic density of dark matter. The regions excluded by LUX (XENON1T) experiment are delineated with dashed blue (dotted blue) lines and dark (light) shadings. *Left:* A close-up of the resonant annihilation region, $m_S \sim m_h/2$. The pink shaded region is excluded at 2σ CL by an upper limit of 19% on $\mathcal{BR}(h \rightarrow SS)$. *Right:* The full mass range of m_S .

to be in tension with current indirect searches at slightly more than 1σ CL. The same is true when $m_S \lesssim 50.8$ GeV, however this region is currently excluded by the Higgs invisible width constraint at more than 2σ CL. In extending the current indirect search limits to high scalar masses, we find that scalar masses up to ~ 240 GeV are excluded by the current indirect DM searches at more

than 1σ CL.

The combined future limits incorporate the Planck polarization data, $\gtrsim 100$ hrs GC observation by CTA and extended improvements in the Fermi-LAT data from the addition of more southern dwarf galaxies in its search. Due mainly to better exposure, future indirect DM searches will be sensitive enough to probe higher scalar DM masses, if S makes up all of the dark matter. At low scalar masses, the future DM searches are relatively insensitive to the assumed DM halo profile (Einasto or a contracted NFW). This is mainly due to the fact that the Fermi log-likelihood dominates in this regime. However, at higher scalar masses, the CTA-log-likelihood entering in Eq. (28) gives the dominant contribution in the total-likelihood. Hence, the upcoming CTA experiment will be able to exclude scalar masses up to 5 TeV (for a contracted NFW profile) and 1.6 TeV (for the Einasto profile) at more than 90% CL, if S makes up all of dark matter.

The resulting limits in the (m_S, λ_{hS}) plane from the LUX (blue dashed) and projected XENON1T (blue dotted) experiment are shown in Fig. 4. In the left-panel near the resonance $m_S \sim m_h/2$, a small triangle will continue to evade detection at LUX and projected XENON1T experiments. At higher scalar masses, the LUX experiment exclude scalar masses up to 120 GeV for a narrow range of λ_{hS} values. Most of the remaining parameter space will be tested and ruled out by the XENON1T experiment for a wide range of couplings λ_{hS} . In particular, it will be able to exclude scalar masses up to 10 TeV, if S makes up all of the dark matter.

B. Vector model

The contours of fixed vector relic density $(\Omega_V h^2)$ for $f_{\text{rel}} = 1$ (black solid), 0.1 (red dashed) and 0.01 (blue dotted) are shown in Fig. 5. For $f_{\text{rel}} = 0.1$ (0.01), no values of λ_{hV} satisfy Eq. (18) below 46 (56) GeV. The minimum relic density below these vector masses stays above the values of the contour being drawn, thereby leaving gaps which are evident in the left-panel of Fig. 5.

In the region $m_V < m_h/2$, an upper limit of 19% (pink solid) at 2σ CL and 5% (pink dotted) at 1σ CL on the Higgs invisible branching $\mathcal{BR}(h \rightarrow VV)$ exclude couplings larger than $\log_{10} \lambda_{hV} \sim -2.28$ and $\log_{10} \lambda_{hV} \sim -2.6$ respectively. The combined constraints on the vector relic density and the Higgs invisible width excludes most of the low vector masses apart from a small triangle between 56.5 GeV and $m_h/2$. Above $m_V > m_h/2$, the relic density contours scale linearly with $\log_{10} m_V$ in a similar fashion to the scalar model.

The combined sensitivity of indirect searches to various regions in the (m_V, λ_{hV}) plane are shown in Fig. 6. The current limits involve contributions from WMAP7 and the combined analysis

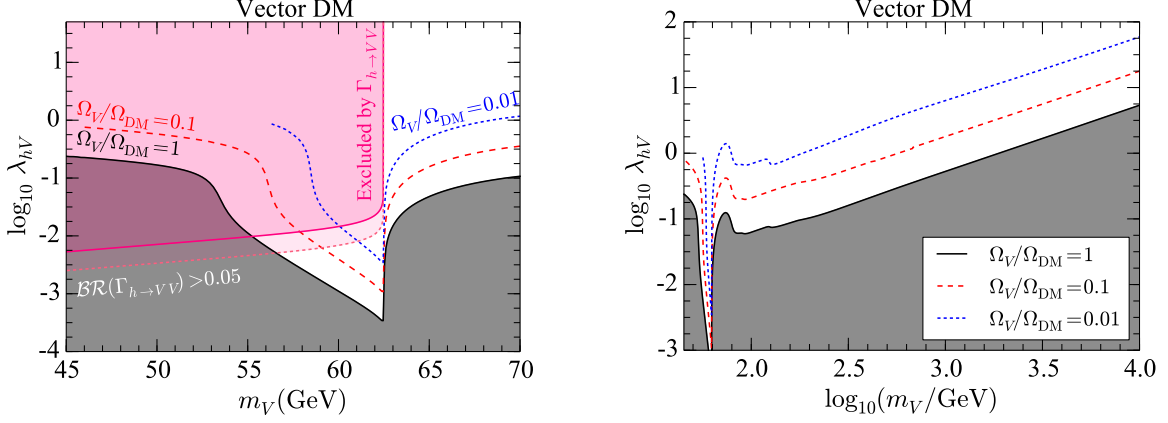


FIG. 5: Contours of fixed vector relic density for $f_{\text{rel}} = 1$ (black solid), 0.1 (red dashed) and 0.01 (blue dotted). The grey shaded region is excluded due to an overabundance of dark matter. *Left*: A close-up of the region $m_V \sim m_h/2$ where annihilations are resonantly enhanced. Larger values of λ_{hV} are excluded by an upper limit of 19% (pink solid) at 2σ CL or 5% (pink dotted) at 1σ CL on $\mathcal{BR}(h \rightarrow VV)$. *Right*: Relic density contours for the full range of m_V .

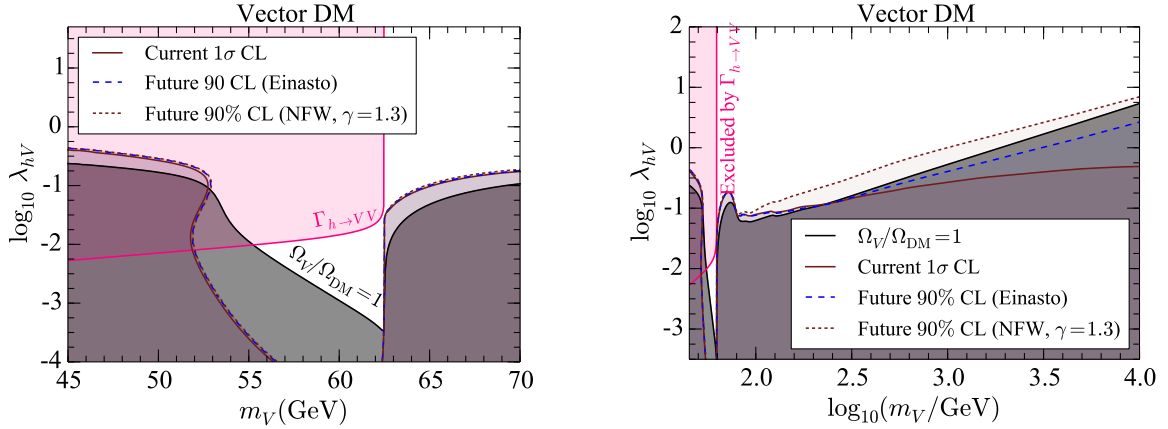


FIG. 6: Indirect search limits on the vector model parameter space. The grey and pink shaded regions are excluded respectively by the observed DM relic density and an upper limit of 19% on $\mathcal{BR}(h \rightarrow VV)$. Values of λ_{hV} below the current 1σ CL (brown solid) curve are excluded at more than 1σ CL. Regions below the future 90% CL curve with the Einasto (blue dashed) and contracted NFW (brown dotted) profiles will be excluded. *Left*: A close-up of the resonant annihilation region, $m_V \sim m_h/2$. *Right*: The full range of m_V .

of 15 dwarfs by Fermi-LAT. The region $m_h/2 \leq m_V \leq 70$ GeV with $\log_{10} \lambda_{hV} \in [-2.5, -0.75]$ can be seen to be in tension with current indirect searches. The same is true at vector masses below ~ 52.5 GeV, however this region is already excluded by the Higgs invisible width constraint at more than 2σ CL. Vector masses up to ~ 300 GeV are excluded at more than 1σ CL by the

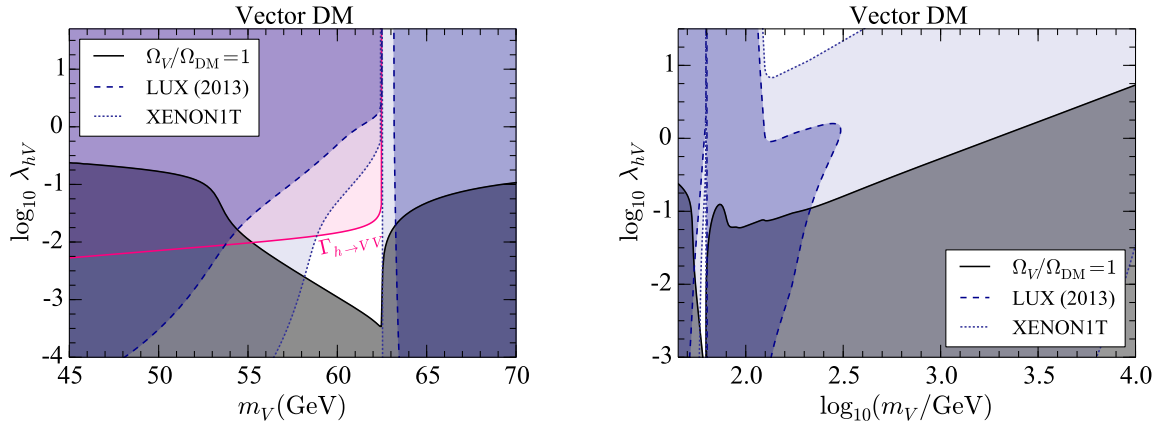


FIG. 7: Direct search limits on the vector model parameter space. The grey shaded region is ruled out by the observed relic density of dark matter. The regions excluded by LUX (XENON1T) experiment are delineated with dashed blue (dotted blue) lines and dark (light) shadings. *Left*: A close-up of the region annihilation region, $m_V \sim m_h/2$. The pink shaded region is excluded by an upper limit of 19% on $\mathcal{BR}(h \rightarrow VV)$. *Right*: The full mass range of m_V .

current indirect DM searches.

Limits from future indirect DM searches will be able to probe parts of the parameter space that are not already excluded by either the current indirect searches or the relic density constraints. In particular, future searches based on the Einasto and a contracted NFW DM profiles will exclude vector masses up to ~ 300 GeV and ~ 14 TeV respectively at more than 90% CL, if V makes up all of the dark matter.

In Fig. 7 Limits from the LUX (blue dashed) and projected XENON1T (blue dotted) experiments in the (m_V, λ_{hV}) plane are shown. The LUX experiment can exclude vector masses up to ~ 300 GeV for a moderate range of λ_{hV} values. The projected XENON1T experiment will exclude most parts of the parameter space that are not presently ruled out by the combined relic density and Higgs invisible width constraints. In particular, it will be able to exclude vector masses up to ~ 30 TeV, if V makes up all of the dark matter.

C. Majorana fermion model

The contours of fixed Majorana relic density in the $(m_\chi, \lambda_{h\chi}/\Lambda_\chi)$ plane for $f_{\text{rel}} = 1$ (black solid), 0.1 (red dashed) and 0.01 (blue dotted) are shown in Fig. 8. Contours in each row are generated at fixed values of $\cos \xi$: $\cos \xi = 1$ for a pure scalar interaction (top row); $\cos \xi = 1/\sqrt{2}$ for an equal mix between the scalar and pseudoscalar terms (middle row); $\cos \xi = 0$ for a pure pseudoscalar

interaction (bottom row). As the interactions between the SM Higgs and the Majorana fermion DM change from pure scalar to pure pseudoscalar in nature, the Majorana relic density contours move to lower values of $\lambda_{h\chi}/\Lambda_\chi$.

In the region $m_\chi < m_h/2$, most values of $\lambda_{h\chi}/\Lambda_\chi$ for $\cos \xi = 1, 1/\sqrt{2}$ and 0 are excluded by the combined constraints on the Majorana relic density and the Higgs invisible width apart from a small triangle that continues to evade these limits in a similar fashion to the scalar and vector models. Above Majorana masses of ~ 300 GeV, the relic density contours for $\cos \xi = 1/\sqrt{2}$ or 0 essentially remain constant and independent of the coupling $\lambda_{h\chi}/\Lambda_\chi$.

The combined sensitivity of indirect searches to various regions in the $(m_\chi, \lambda_{h\chi}/\Lambda_\chi)$ plane is shown in Fig. 9 for $\cos \xi = 1$ (top row), $1/\sqrt{2}$ (middle row) and 0 (bottom row). For the case of $\cos \xi = 1$, the annihilation cross-section σv_{rel} entering in the calculation of indirect detection rates receive a v^2 suppression where $v \sim 10^{-3} c$ is the typical speed of dark matter in a local halo. Consequently, the indirect search limits are weak and no exclusion is possible when $m_\chi < m_h/2$.

When interactions become pure pseudoscalar in nature, the velocity suppression of σv_{rel} is lifted. Consequently, the indirect search limits are non-trivial. For the case of $\cos \xi = 1/\sqrt{2}$ and 0, Majorana masses between $m_h/2$ and 70 GeV with $\log_{10}(\lambda_{h\chi}/\Lambda_\chi \text{ GeV}) \in [-4.1, -2.8]$ can be seen to be in tension with the current indirect searches at more than 1σ CL. Analogous to the indirect limits in the scalar and vector models, a small region around $m_\chi \lesssim m_h/2$ will continue to evade the current and future indirect searches. Future indirect searches will be sensitive enough to exclude Majorana masses up to ~ 200 GeV (for the Einasto profile) and ~ 5 TeV (for a contracted NFW profile) at more than 90% CL, if χ makes up all of the dark matter.

In Fig. 10, we present limits from LUX (blue dashed) and projected XENON1T (blue dotted) experiments in the $(m_\chi, \lambda_{h\chi}/\Lambda_\chi)$ plane for $\cos \xi = 1$ (top row), $1/\sqrt{2}$ (middle row) and 0 (bottom row). When $\cos \xi = 0$, the SI cross-section is momentum suppressed by a factor of $q^2/4m_\chi^2$. Since the momentum transfer q in a typical DM-nucleus interaction is small relative to the mediator mass m_h , the expected number of signal events (s) is small. In fact, the imposed direct search constraints are significantly weaker than the Higgs invisible width constraints at 2σ CL. Hence, the higher Majorana mass range with pure pseudoscalar coupling (i.e., $\cos \xi = 0$) will be inaccessible at the XENON1T experiment.

When interactions are pure scalar in nature, the momentum suppression is lifted from the SI cross-section. In the case of an equal mixing, ($\cos \xi = 1/\sqrt{2}$), although the DM-nucleon effective couplings ($G_N^{\text{SI}}, \tilde{G}_N^{\text{SI}}$) are equal, the pseudoscalar effective couplings (\tilde{G}_N^{SI}) carry a momentum dependence as evident in Eq. (44). Consequently, the direct search limits are strongest for the case

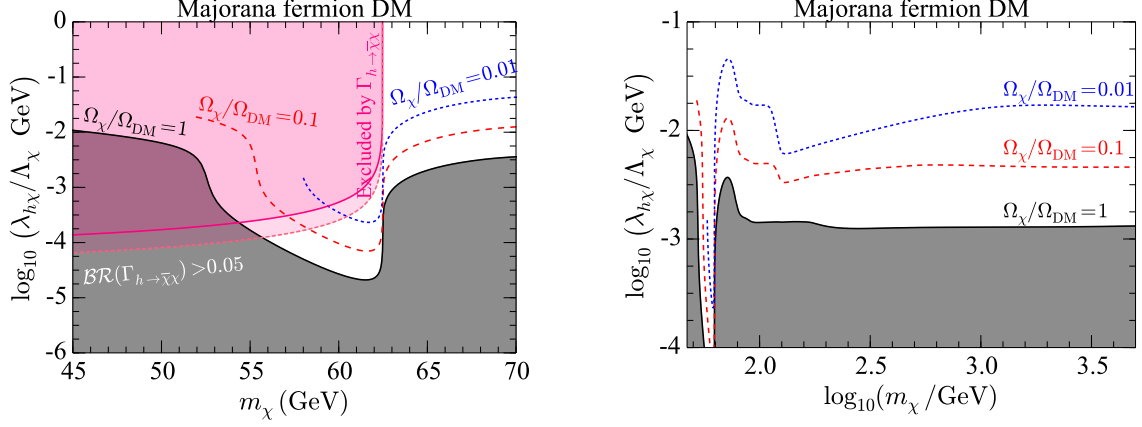
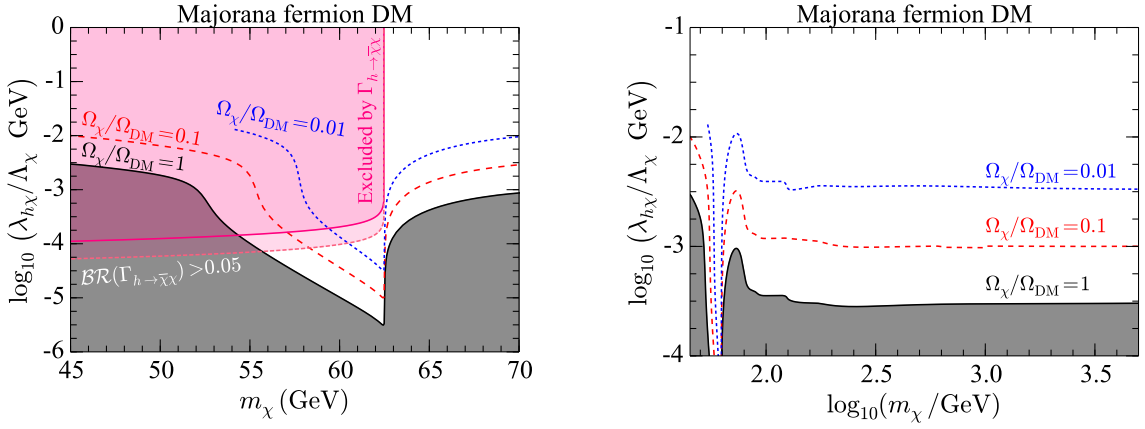
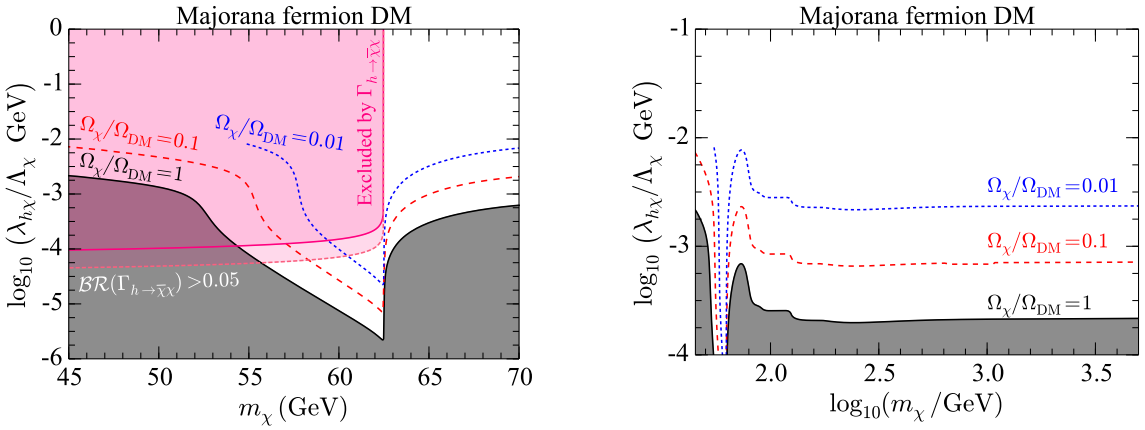
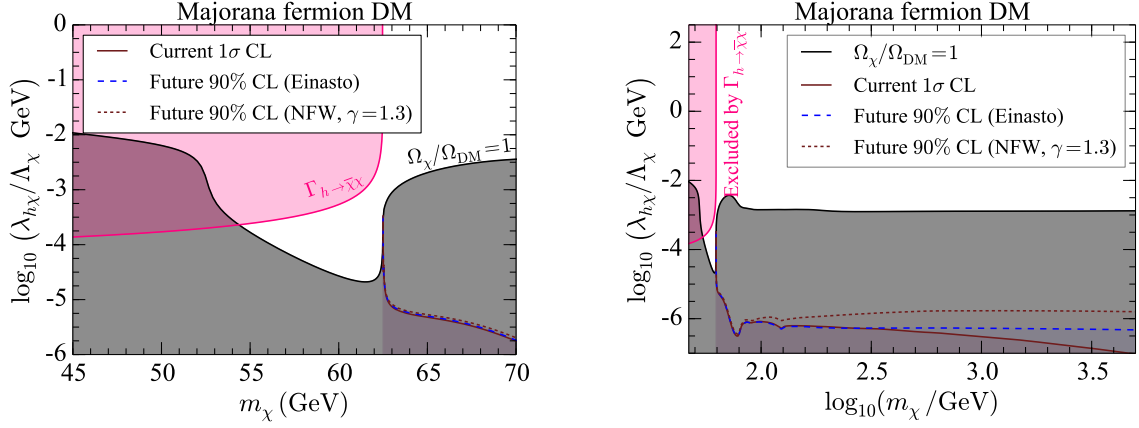
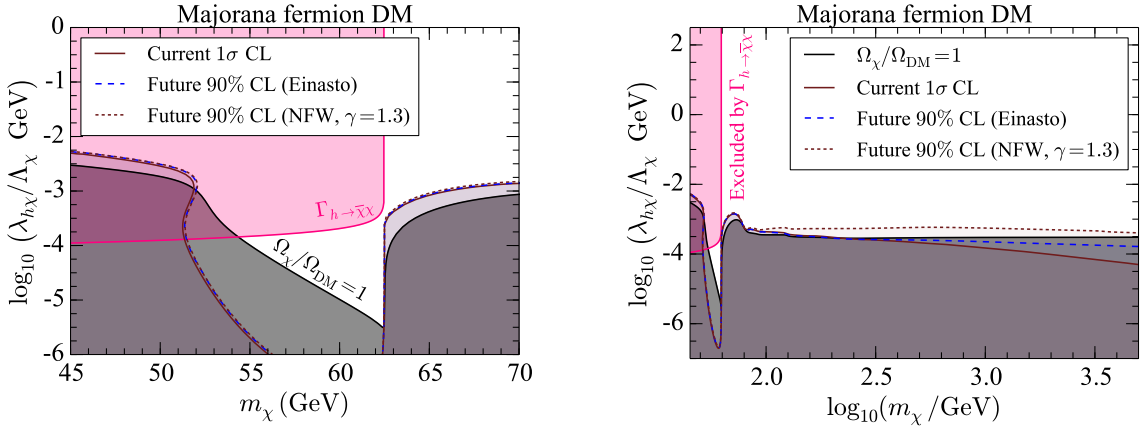
a). Pure scalar interaction, $\cos \xi = 1$.b). Equally mixed scalar-pseudoscalar interaction, $\cos \xi = 1/\sqrt{2}$.c). Pure pseudoscalar interaction, $\cos \xi = 0$.

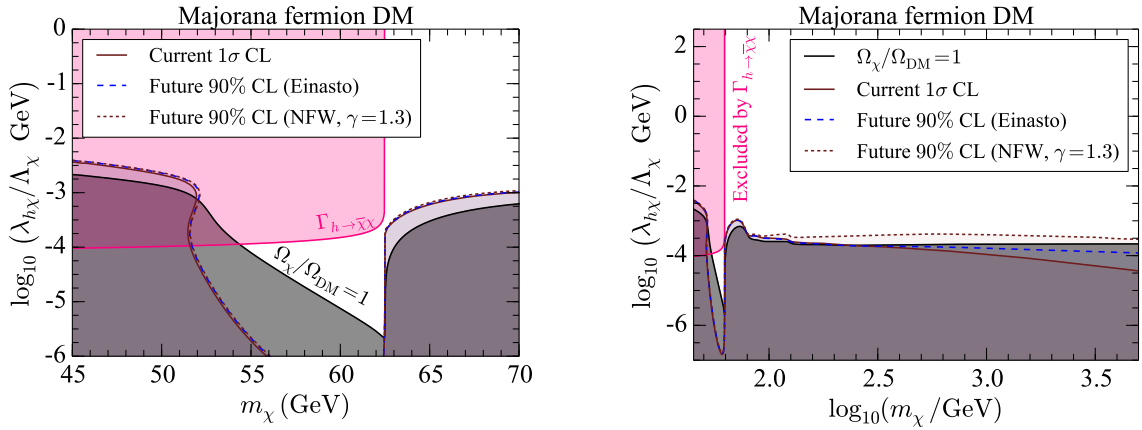
FIG. 8: Contours of fixed Majorana relic density for $f_{\text{rel}} = 1$ (black solid), 0.1 (red dashed) and 0.01 (blue dotted). The grey shaded region is ruled out by due to an overabundance of dark matter. *Left*: A close-up of the resonant annihilation region, $m_\chi \sim m_h/2$. Large values of $\lambda_{h\chi}/\Lambda_\chi$ are excluded by an upper limit of 19% (pink solid) at 2σ CL or 5% (pink dotted) at 1σ CL on $\mathcal{BR}(h \rightarrow \bar{\chi}\chi)$. *Right*: Relic density contours for the full range of m_χ .



a). Pure scalar interaction, $\cos \xi = 1$.



b). Equally mixed scalar-pseudoscalar interaction, $\cos \xi = 1/\sqrt{2}$.



c). Pure pseudoscalar interaction, $\cos \xi = 0$.

FIG. 9: Indirect search limits on the Majorana model parameter space. The grey and pink shaded regions are excluded respectively by the relic density and the Higgs invisible width constraints. Values of $\lambda_{h\chi}/\Lambda_\chi$ below the current 1σ CL (brown solid) curve are excluded at more than 1σ CL. Regions below the future 90% CL curve with the Einasto (blue dashed) and contracted NFW (brown dotted) profiles will be excluded. *Left*: A close-up of the resonant annihilation region, $m_\chi \sim m_h/2$. *Right*: The full range of m_χ .

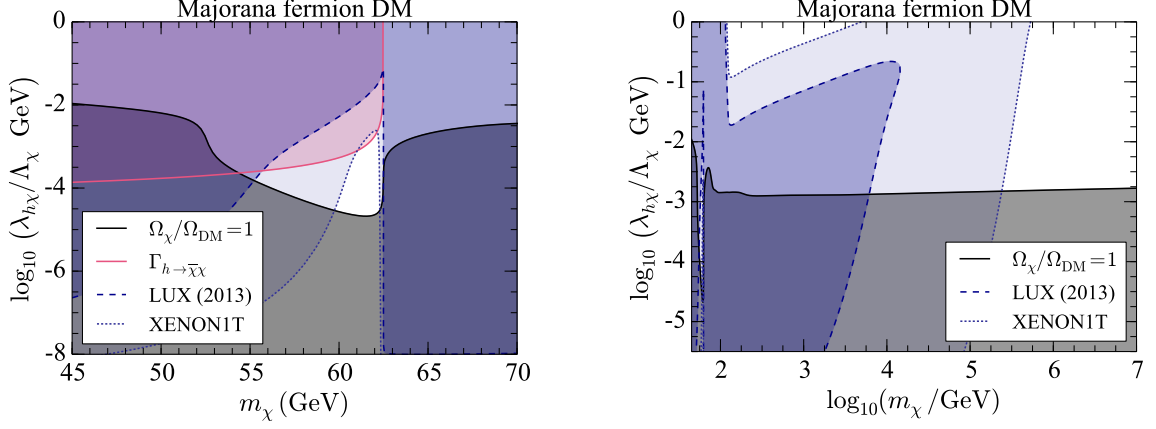
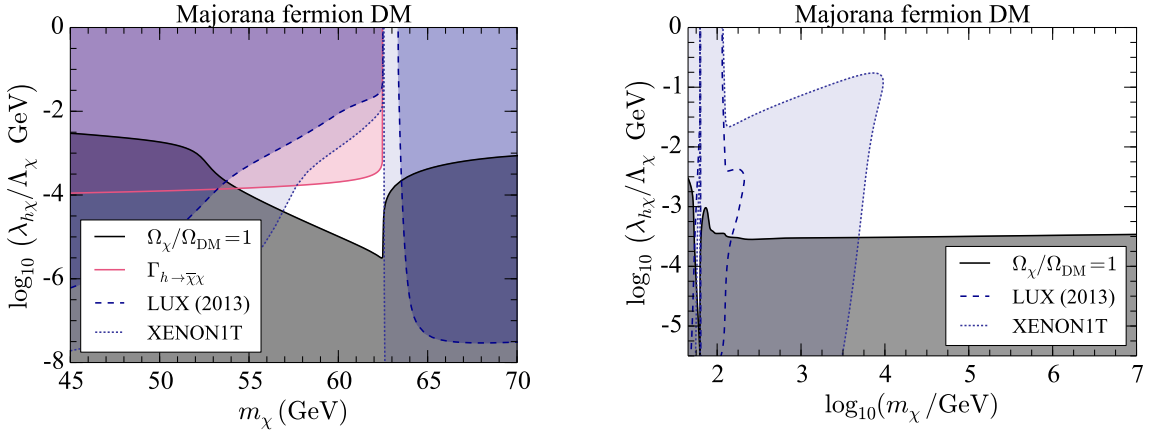
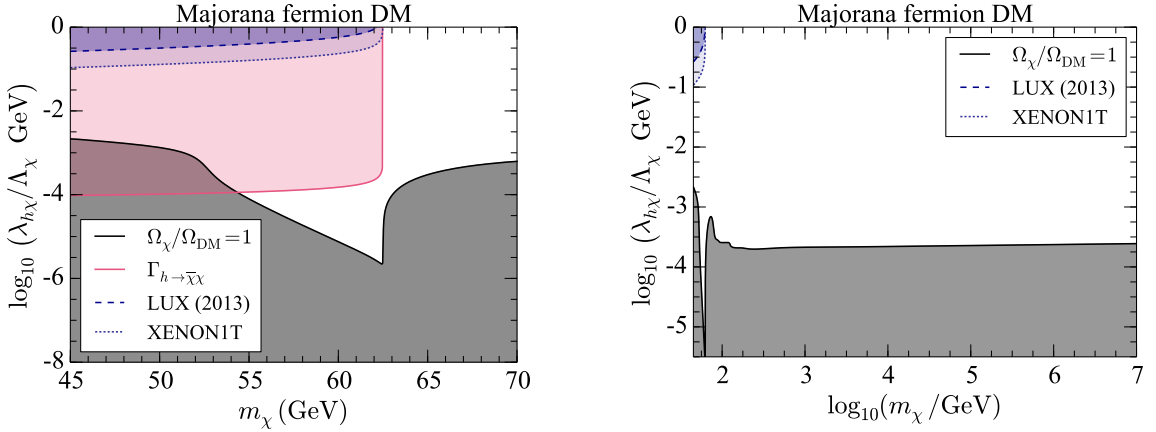
a). Pure scalar interaction, $\cos \xi = 1$.b). Equally mixed scalar-pseudoscalar interaction, $\cos \xi = 1/\sqrt{2}$.c). Pure pseudoscalar interaction, $\cos \xi = 0$.

FIG. 10: Direct search limits on the Majorana model parameter space. The grey shaded region is ruled out by the relic density constraint. The regions excluded by LUX (XENON1T) experiment are delineated with dashed blue (dotted blue) lines and dark (light) shadings. *Left*: A close-up of the resonant annihilation region, $m_\chi \sim m_h/2$. The pink shaded region is excluded by an upper limit of 19% on $\text{BR}(h \rightarrow \bar{\chi}\chi)$. *Right*: The full mass range of m_χ .

of a pure scalar interaction and moderate for an equal mix of scalar and pseudoscalar terms.

At Majorana masses above 70 GeV, direct search experiments will exclude large portions of the model parameter space. The LUX experiment excludes Majorana masses up to ~ 14 TeV when $\cos \xi = 1$ and ~ 200 GeV when $\cos \xi = 1/\sqrt{2}$. Further exclusion will be also be possible with the projected XENON1T experiment.

For the case of $\cos \xi = 0$, no direct limits can be imposed due to the momentum suppression of the SI cross-section. This coincides with better prospects from indirect detection (bottom row in Fig. 9), making the latter class of observation the *only* type of experiment capable of probing the high DM mass range should nature have chosen to have dark matter interact with the SM Higgs boson only by a pure pseudoscalar coupling.

D. Dirac fermion model

The Dirac fermion model is similar to the Majorana fermion model. One aspect that separates Majorana fermion from Dirac fermion dark matter is the conventional factor of $1/2$ in front of each fermion bilinear $\bar{\psi}\psi$ in defining a Majorana fermion field χ . This factor of $1/2$ accounts for the field normalisation and self-conjugation. The Majorana model results carry over to the Dirac model in a relatively straightforward way after this factor of $1/2$ is accounted for.

In Fig. 11, we show our fixed Dirac relic density contours in $(m_\psi, \lambda_{h\psi}/\Lambda_\psi)$ plane for $f_{\text{rel}} = 1$ (black solid), 0.1 (red dashed) and 0.01 (blue dotted). Analogous to the Majorana model, contours in each row are generated at fixed values of $\cos \xi$: $\cos \xi = 1$ for a pure scalar interaction (top row); $\cos \xi = 1/\sqrt{2}$ for an equal mix between the scalar and pseudoscalar terms (middle row); $\cos \xi = 0$ for a pure pseudoscalar interaction (bottom row). For $m_\psi < m_h/2$, most of the parameter space except a small triangular region between ~ 57.5 GeV and $m_h/2$ is excluded by the combined constraints on the Dirac relic density and the Higgs invisible width. Similar to the Majorana model, roots of Eq. (18) do not exist at Dirac masses below $m_h/2$ for $f_{\text{rel}} = 0.1$ and 0.01. Above $m_\psi > m_h$, the relic density contours continue to increase and ultimately become independent of the coupling $\lambda_{h\psi}/\Lambda_\psi$.

The sensitivity of indirect search experiments to various regions in the $(m_\psi, \lambda_{h\psi}/\Lambda_\psi)$ plane when $\cos \xi = 1$ (top row), $1/\sqrt{2}$ (middle row) and 0 (bottom row) is shown in Fig. 12. Again, in the case $\cos \xi = 1$, the annihilation cross-section σv_{rel} is velocity suppressed. Consequently, indirect search limits are weak. In fact, the relic density constraint alone is strong enough to exclude the entire region probed by the indirect search experiments.

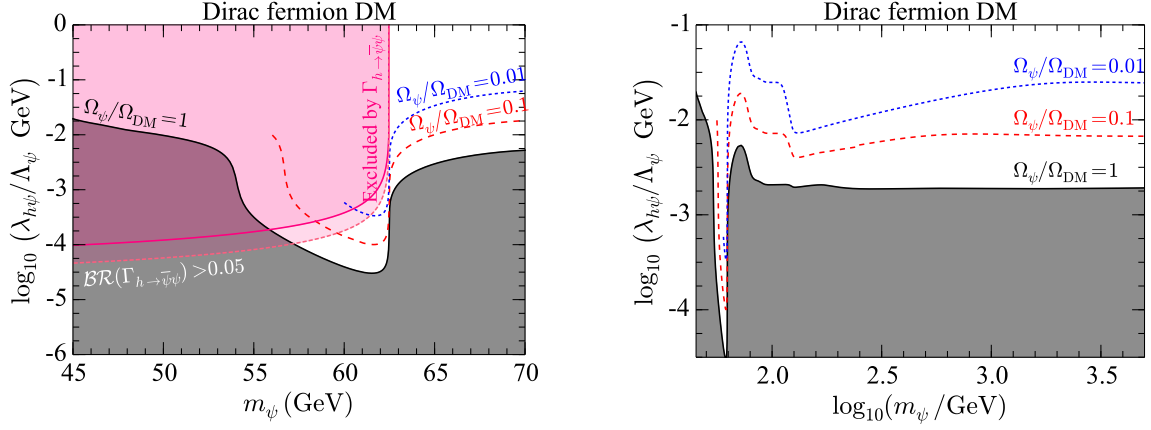
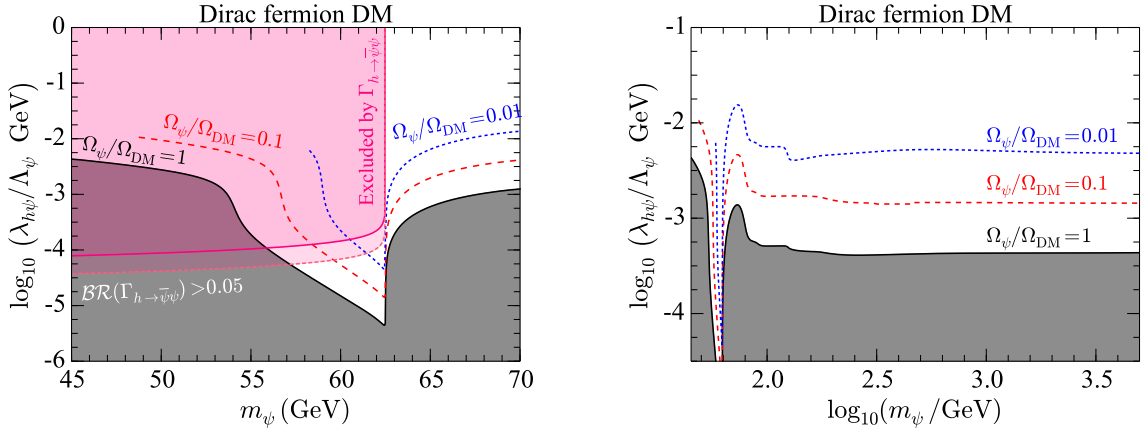
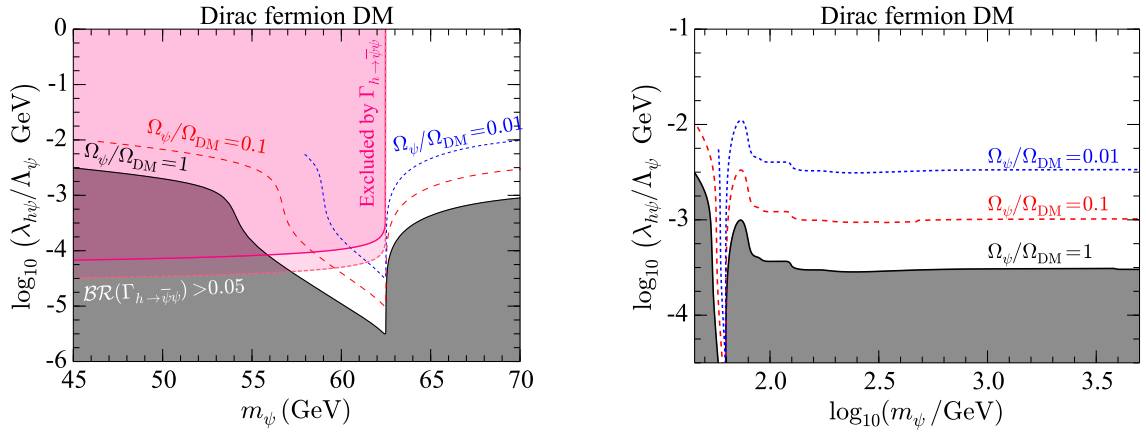
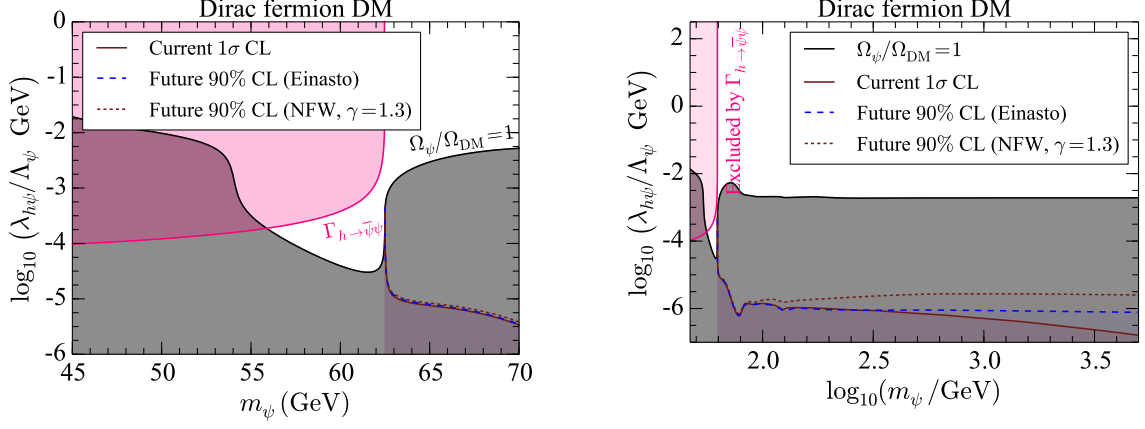
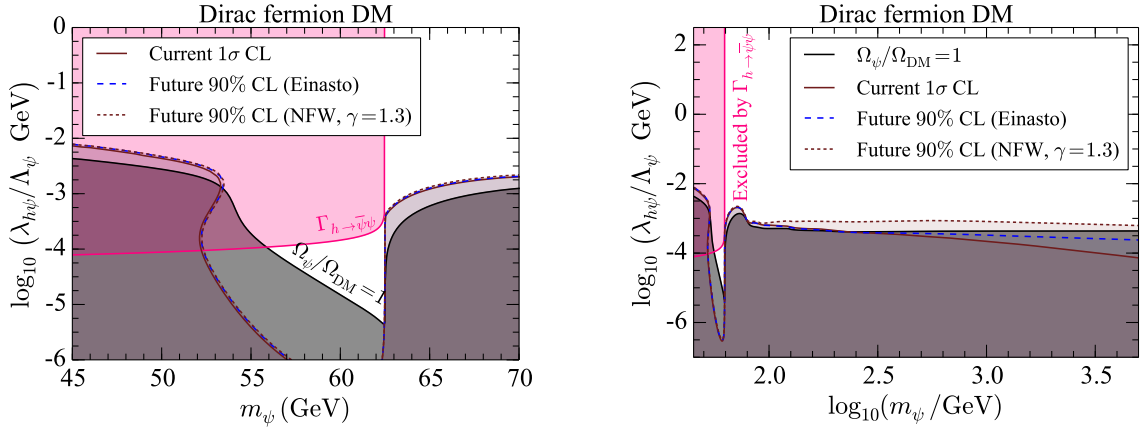
a). Pure scalar interaction, $\cos \xi = 1$ b). Equally mixed scalar-pseudoscalar interaction, $\cos \xi = 1/\sqrt{2}$.c). Pure pseudoscalar interaction, $\cos \xi = 0$.

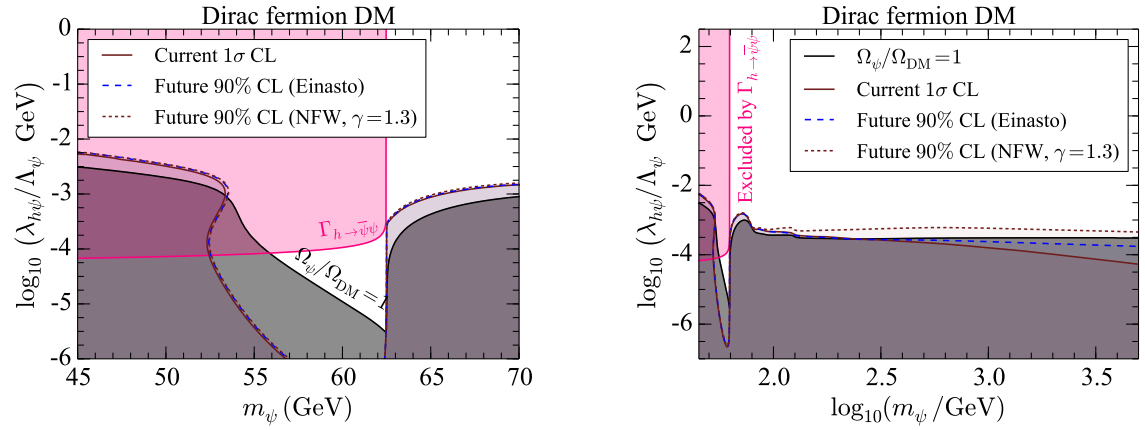
FIG. 11: Contours of fixed Dirac relic density for $f_{\text{rel}} = 1$ (black solid), 0.1 (red dashed) and 0.01 (blue dotted). The grey shaded region is ruled out due to an overabundance of dark matter. *Left*: A close-up of the resonant annihilation region, $m_\psi \sim m_h/2$. Large values of $\lambda_{h\psi}/\Lambda_\psi$ are excluded by an upper limit of 19% (pink solid) at 2σ CL or 5% (pink dotted) at 1σ CL on $\mathcal{BR}(h \rightarrow \bar{\psi}\psi)$. *Right*: Relic density contours for the full range of m_ψ .



a). Pure scalar interaction, $\cos \xi = 1$.



b). Equally mixed scalar-pseudoscalar interaction, $\cos \xi = 1/\sqrt{2}$.



c). Pure pseudoscalar interaction, $\cos \xi = 0$.

FIG. 12: Indirect search limits on the Dirac model parameter space. The grey and pink shaded regions are excluded respectively by the relic density and the Higgs invisible width constraints. Values of $\lambda_{h\psi}/\Lambda_\psi$ below the current 1σ CL (brown solid) curve are excluded at more than 1σ CL. Regions below the future 90% CL curve with the Einasto (blue dashed) and contracted NFW (brown dotted) profiles will be excluded. *Left*: A close-up of the resonant annihilation region, $m_\psi \sim m_h/2$. *Right*: The full range of m_ψ .

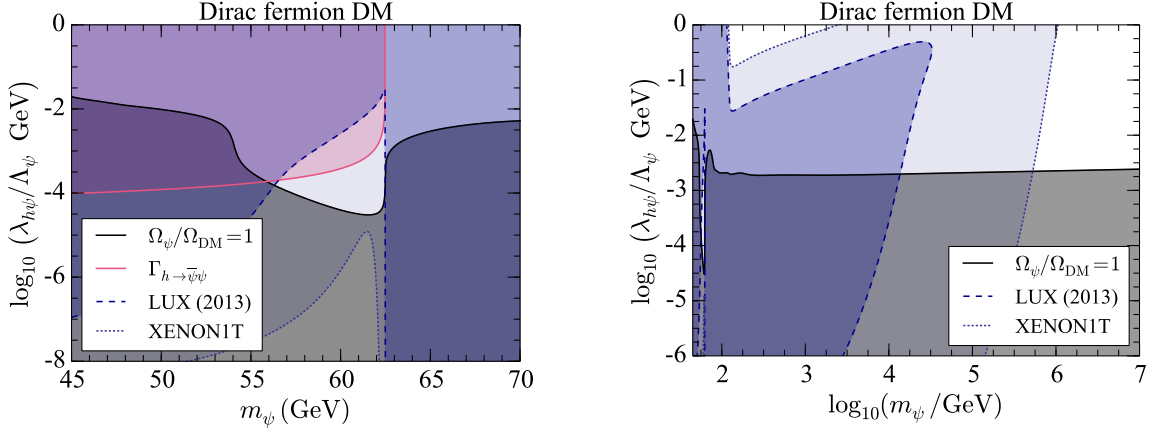
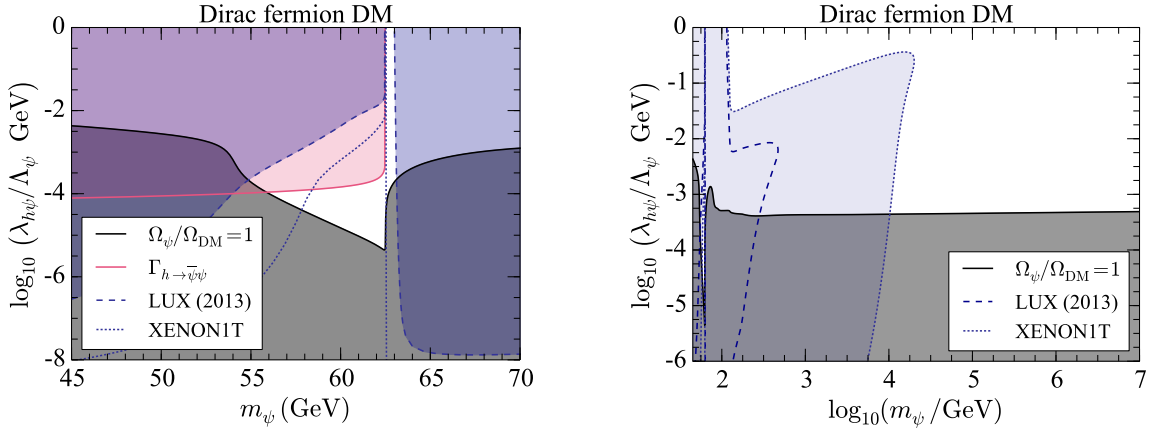
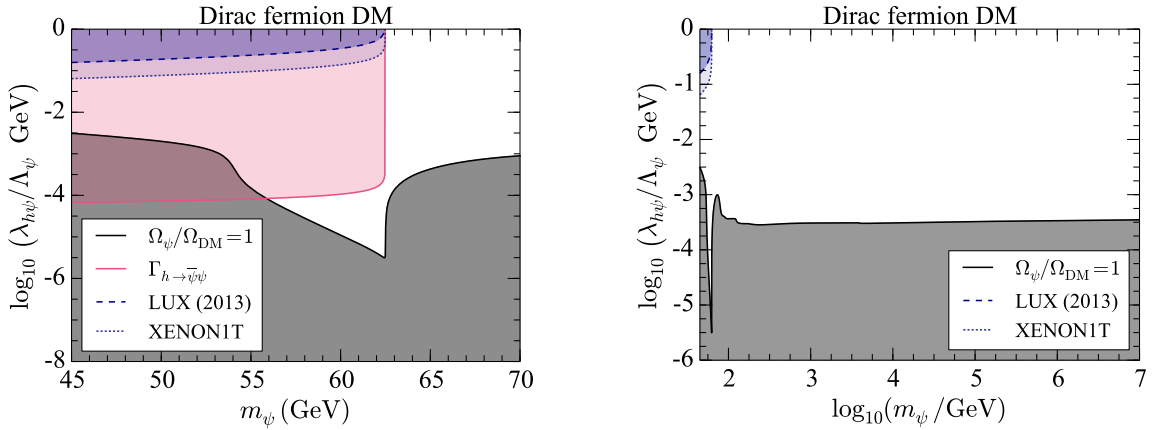
a). Pure scalar interaction, $\cos \xi = 1$.b). Equally mixed scalar-pseudoscalar interaction, $\cos \xi = 1/\sqrt{2}$.c). Pure pseudoscalar interaction, $\cos \xi = 0$.

FIG. 13: Direct search limits on the Dirac model parameter space. The grey shaded region is ruled out by the relic density constraint. The regions excluded by LUX (XENON1T) experiment are delineated with dashed blue (dotted blue) lines and dark (light) shadings. *Left:* A close-up of the resonant annihilation region, $m_\psi \sim m_h/2$. The pink shaded region is excluded by an upper limit of 19% on $\mathcal{BR}(h \rightarrow \bar{\psi}\psi)$. *Right:* The full mass range of m_ψ .

As interactions change towards pure pseudoscalar in nature, the velocity suppression of σv_{rel} is lifted. Therefore, parts of the parameter space can be excluded by indirect search experiments. With the strongest indirect limits in the case of a pure scalar interaction, Dirac masses between $m_h/2$ and 70 GeV for $\log_{10}(\lambda_{h\psi}/\Lambda_\psi \text{ GeV}) \in [-4, -3]$ can be seen to be in tension with current indirect limits which incorporate the combined analysis of 15 dwarf galaxies by Fermi-LAT and 7-years observation of the CMB (WMAP7). Above $m_\psi > m_h/2$, limits from future indirect searches will exclude Dirac masses up to ~ 230 GeV for the Einasto profile and ~ 4 TeV for a contracted NFW profile, if ψ makes up all of dark matter.

In Fig. 13, we present direct detection limits in the $(m_\psi, \lambda_{h\psi}/\Lambda_\psi)$ plane for $\cos \xi = 1$ (top row), $1/\sqrt{2}$ (middle row) and 0 (bottom row). For the case $\cos \xi = 0$, the SI cross-section entering in Eq. (38) is momentum suppressed by a factor of $q^2/4m_\psi^2$. Consequently, the expected event rates are small. In contrast with the Majorana model when $\cos \xi = 1$, Dirac fermion masses between 45 GeV and $m_h/2$ will be entirely excluded by the combined constraints on the Dirac relic density, the Higgs invisible width and projected XENON1T experiment.

As interactions change to pure scalar in nature, the suppression of the SI cross-section is lifted and therefore the expected event rates become significant. The LUX experiment excludes Dirac masses up to ~ 32 TeV when $\cos \xi = 1$ and ~ 450 GeV when $\cos \xi = 1/\sqrt{2}$. In the near future, the projected XENON1T experiment will reach higher sensitivity in excluding TeV-scale Dirac masses, if ψ makes up all of the dark matter.

In analogy with the Majorana model with $\cos \xi = 0$, no direct search limits can be imposed on the Dirac fermion parameter space due of the momentum-suppression of the SI cross-section. Better prospects from indirect detection (bottom row in Fig. 12) makes the latter class of observation the *only* type of experiment capable of probing the high DM mass range if nature have chosen to have dark matter interact with the SM Higgs boson only by a pure pseudoscalar coupling.

V. CONCLUSIONS

In this work, we have updated and performed a combined analysis of effective scalar, vector, Majorana and Dirac fermion Higgs portal models of dark matter. For the fermion models, we investigated cases where interactions are either pure scalar, pure pseudoscalar or an equal mixture of the scalar and pseudoscalar terms. The presence of the pseudoscalar term and the requirement of a quadratic DM term corresponding to a real mass lead us to redefine the post-EWSB fermion fields through a chiral rotation.

In non-fermion models, the combined limits on the relic density and the Higgs invisible width exclude most of the low mass parameter space in all models apart for a small triangular region close to the resonance $m_X \sim m_h/2$. However, in the special case of a Dirac fermion DM interacting with the SM Higgs via a pure scalar coupling, the entire resonance region will be excluded by the projected XENON1T experiment.

For the first time, we have performed a consistent study of the indirect detection prospects in all four effective Higgs portal models. Using current and future gamma-ray astronomy data, we looked for the viable regions of parameter space that can be probed by existing or future indirect searches. Below the resonance $m_X \sim m_h/2$, the indirect search limits are weaker than the combined constraints on the relic density and the Higgs invisible width. However, at higher DM masses, indirect limits can provide stronger exclusions in most regions of the parameter space where the model comprises all of dark matter. Strong exclusions at high DM masses can be placed in the case of a contracted NFW halo profile. The forthcoming CTA experiment will be very useful in searching for signs of DM annihilation.

In agreement with similar studies performed elsewhere, direct search experiments will continue to provide the strongest limits on the parameter space in all models. The projected XENON1T experiment for instance, will have the sensitivity to probe TeV-scale DM masses. Since previous studies on fermionic DM models with a pure pseudoscalar interaction have naively applied XENON100 and/or LUX limits without properly taking accounting of the momentum suppressed SI cross-section, we have re-derived these limits by including the proper momentum-dependence of the form $q^2/4m_X^2$ in our calculations. The resulting limits, although weak, are important in order to perform a consistent study of these effective models.

In fermion models with pure pseudoscalar coupling with the SM Higgs, the momentum suppression of the SI cross-section gives suppressed detection rates, thereby making the direct detection of these models difficult. Indirect search experiments are therefore our *only* hope of accessing the higher DM mass range of these models.

When both the indirect and direct search limits are available as in our portal models, a joint observation is possible at higher WIMP masses. A detection in multiple experiments would provide a far more robust discovery than a single signal alone.

ACKNOWLEDGMENTS

We thank Csaba Balazs, Jim Cline, Alexander Pukhov and Geneviève Bélanger for useful discussions. AB would like to thank Andre Scaffidi for his assistance during the `LUXCalc` package setup. The work of AB, FR and AW is supported by the ARC Centre of Excellence for Particle Physics at the Terascale (CoEPP) and the Centre for the Subatomic Structure of Matter (CSSM). MW is supported by the Australian Research Council Future Fellowship FT140100244. PS is supported by the STFC through the Ernest Rutherford Fellowships scheme.

Appendix A: Chiral Rotation

1. Dirac fermion model

We start with the post-EWSB Lagrangian for the Dirac fermion DM field ψ of

$$\mathcal{L}_\psi = \mathcal{L}_{\text{SM}} + \bar{\psi} i \not{\partial} \psi - \left[\mu_\psi \bar{\psi} \psi + \frac{1}{2} \frac{\lambda_{h\psi}}{\Lambda_\psi} v_0^2 \left(\cos \theta \bar{\psi} \psi + \sin \theta \bar{\psi} i \gamma_5 \psi \right) \right] - \frac{\lambda_{h\psi}}{\Lambda_\psi} \left(\cos \theta \bar{\psi} \psi + \sin \theta \bar{\psi} i \gamma_5 \psi \right) \left(v_0 h + \frac{1}{2} h^2 \right).$$

The square bracket term in the above expression contains a DM mass-type term and a pseudoscalar coupling of the DM field to the EWSB vacuum v_0 . However, it is convenient to remove the latter term ($\propto \sin \theta$) using a field redefinition through a chiral rotation of the field ψ as

$$\psi \longrightarrow \exp(i\gamma_5 \alpha/2) \psi, \quad \bar{\psi} \longrightarrow \bar{\psi} \exp(i\gamma_5 \alpha/2), \quad (\text{A1})$$

where α is a real parameter independent of space-time.

After expanding the exponential in terms of $\cos \alpha/2$, $\sin \alpha/2$ and using the properties of γ_5 matrix in the Dirac-representation, the exponentials become

$$\exp(i\gamma_5 \alpha/2) = \cos(\gamma_5 \alpha/2) + i \sin(\gamma_5 \alpha/2) = \cos(\alpha/2) + i \gamma_5 \sin(\alpha/2),$$

where the property: $\gamma_5^n = \gamma_5$ ($\mathbb{I}_{4 \times 4}$) for n odd (even) is used.

Under the chiral rotation in Eq. (A1), the term $\bar{\psi} i \not{\partial} \psi$ is invariant since

$$\begin{aligned} \bar{\psi} i \not{\partial} \psi &= \bar{\psi} i \gamma^\mu \partial_\mu \psi \longrightarrow \bar{\psi} \exp(i\gamma_5 \alpha/2) i \gamma^\mu \partial_\mu (\exp(i\gamma_5 \alpha/2) \psi) \\ &= \bar{\psi} \exp(i\gamma_5 \alpha/2) \gamma^\mu \exp(i\gamma_5 \alpha/2) i \partial_\mu \psi \\ &= \bar{\psi} \exp(i\gamma_5 \alpha/2) \exp(-i\gamma_5 \alpha/2) i \gamma^\mu \partial_\mu \psi \quad \left(\{ \gamma_5, \gamma^\mu \} = 0 \right) \\ &= \bar{\psi} i \not{\partial} \psi. \end{aligned}$$

On the contrary, $\bar{\psi}\psi$ and $\bar{\psi}i\gamma_5\psi$ terms transform to

$$\begin{aligned}\bar{\psi}\psi &\longrightarrow \bar{\psi} \exp(i\gamma_5\alpha/2) \exp(i\gamma_5\alpha/2) \psi & \bar{\psi}i\gamma_5\psi &\longrightarrow \bar{\psi} \exp(i\gamma_5\alpha/2) i\gamma_5 \exp(i\gamma_5\alpha/2) \psi \\ &= \bar{\psi} \exp(i\gamma_5\alpha) \psi & &= \bar{\psi} \exp(i\gamma_5\alpha) i\gamma_5 \psi \\ &= \cos \alpha \bar{\psi}\psi + \sin \alpha \bar{\psi}i\gamma_5\psi & &= \cos \alpha \bar{\psi}i\gamma_5\psi - \sin \alpha \bar{\psi}\psi\end{aligned}\quad \left(\gamma_5^2 = \mathbb{I}_{4\times 4}\right)$$

Therefore, terms in the Dirac Lagrangian transform to

$$\begin{aligned}-\mu_\psi \bar{\psi}\psi &\longrightarrow -\left(\mu_\psi \cos \alpha \bar{\psi}\psi + \mu_\psi \sin \alpha \bar{\psi}i\gamma_5\psi\right) \\ \frac{1}{2} \frac{\lambda_{h\psi}}{\Lambda_\psi} v_0^2 \left(\cos \theta \bar{\psi}\psi + \sin \theta \bar{\psi}i\gamma_5\psi\right) &\longrightarrow \frac{1}{2} \frac{\lambda_{h\psi}}{\Lambda_\psi} v_0^2 \left(\cos \theta \cos \alpha \bar{\psi}\psi + \cos \theta \sin \alpha \bar{\psi}i\gamma_5\psi\right. \\ &\quad \left.+ \sin \theta \cos \alpha \bar{\psi}i\gamma_5\psi - \sin \theta \sin \alpha \bar{\psi}\psi\right) \\ &= \frac{1}{2} \frac{\lambda_{h\psi}}{\Lambda_\psi} v_0^2 \left(\cos \xi \bar{\psi}\psi + \sin \xi \bar{\psi}i\gamma_5\psi\right) \\ -\frac{1}{2} \frac{\lambda_{h\psi}}{\Lambda_\psi} \left(\cos \theta \bar{\psi}\psi + \sin \theta \bar{\psi}i\gamma_5\psi\right) &\longrightarrow -\frac{1}{2} \frac{\lambda_{h\psi}}{\Lambda_\psi} \left(\cos \theta \cos \alpha \bar{\psi}\psi + \cos \theta \sin \alpha \bar{\psi}i\gamma_5\psi\right. \\ &\quad \left.+ \sin \theta \cos \alpha \bar{\psi}i\gamma_5\psi - \sin \theta \sin \alpha \bar{\psi}\psi\right) \\ &= -\frac{1}{2} \frac{\lambda_{h\psi}}{\Lambda_\psi} \left(\cos \xi \bar{\psi}\psi + \sin \xi \bar{\psi}i\gamma_5\psi\right)\end{aligned}$$

where we define $\xi \equiv \theta + \alpha$ for future convenience and use the trigonometric identities $\cos \xi = \cos \theta \cos \alpha - \sin \theta \sin \alpha$ and $\sin \xi = \sin \theta \cos \alpha + \cos \theta \sin \alpha$. Therefore, the mass and interaction terms expand to

$$\begin{aligned}-\left[\mu_\psi \bar{\psi}\psi + \frac{1}{2} \frac{\lambda_{h\psi}}{\Lambda_\psi} v_0^2 \left(\cos \theta \bar{\psi}\psi + \sin \theta \bar{\psi}i\gamma_5\psi\right)\right] &\longrightarrow -\left[\mu_\psi \cos \alpha \bar{\psi}\psi + \mu_\psi \sin \alpha \bar{\psi}i\gamma_5\psi\right. \\ &\quad \left.+ \frac{1}{2} \frac{\lambda_{h\psi}}{\Lambda_\psi} v_0^2 \left(\cos \xi \bar{\psi}\psi + \sin \xi \bar{\psi}i\gamma_5\psi\right)\right] \\ &= -\left[\mu_\psi \cos \alpha + \frac{1}{2} \frac{\lambda_{h\psi}}{\Lambda_\psi} v_0^2 \cos \xi\right] \bar{\psi}\psi \\ &\quad -\left[\mu_\psi \sin \alpha + \frac{1}{2} \frac{\lambda_{h\psi}}{\Lambda_\psi} v_0^2 \sin \xi\right] \bar{\psi}i\gamma_5\psi\end{aligned}\quad (\text{A2})$$

$$\begin{aligned}-\frac{1}{2} \frac{\lambda_{h\psi}}{\Lambda_\psi} \left(\cos \theta \bar{\psi}\psi + \sin \theta \bar{\psi}i\gamma_5\psi\right) \left(v_0 h + \frac{1}{2} h^2\right) &\longrightarrow -\frac{1}{2} \frac{\lambda_{h\psi}}{\Lambda_\psi} \left(\cos \xi \bar{\psi}\psi + \sin \xi \bar{\psi}i\gamma_5\psi\right) \\ &\quad \times \left(v_0 h + \frac{1}{2} h^2\right).\end{aligned}\quad (\text{A3})$$

If $\alpha = \pi$, a sign change of the mass and interaction terms in above expressions occur. We can therefore, without any loss of generality take $\mu_\psi > 0$ as long as we preserve the relative signs between the terms.

After the chiral rotation, we demand that the coefficient of $\bar{\psi}i\gamma_5\psi$ in Eq. (A2) vanishes in order to go to the real mass basis. This defines a proper chiral transformation and gives a field mass

after EWSB in terms of the Lagrangian parameters. Setting the coefficient of $\bar{\psi}i\gamma_5\psi$ to zero gives

$$\mu_\psi \sin \alpha = -\frac{1}{2} \frac{\lambda_{h\psi}}{\Lambda_\psi} v_0^2 \sin \xi = -\frac{1}{2} \frac{\lambda_{h\psi}}{\Lambda_\psi} v_0^2 (\cos \theta \sin \alpha + \sin \theta \cos \alpha).$$

Dividing the above expression on both sides by $\cos \alpha$ and rearranging for $\tan \alpha$ gives

$$\tan \alpha = \left(-\frac{1}{2} \frac{\lambda_{h\psi}}{\Lambda_\psi} v_0^2 \sin \theta \right) \left(\mu_\psi + \frac{1}{2} \frac{\lambda_{h\psi}}{\Lambda_\psi} v_0^2 \cos \theta \right)^{-1}, \quad (\text{A4})$$

as stated for the Dirac fermion model in Section II. From the expression for $\tan \alpha$, we can determine $\sin^2 \alpha$ and $\cos^2 \alpha$ as follows

$$\begin{aligned} \cos^2 \alpha &= \frac{1}{1 + \tan^2 \alpha} = \frac{\left(\mu_\psi + \frac{1}{2} \frac{\lambda_{h\psi}}{\Lambda_\psi} v_0^2 \cos \theta \right)^2}{\left(\mu_\psi + \frac{1}{2} \frac{\lambda_{h\psi}}{\Lambda_\psi} v_0^2 \cos \theta \right)^2 + \left(\frac{1}{2} \frac{\lambda_{h\psi}}{\Lambda_\psi} v_0^2 \sin \theta \right)^2}, \\ \sin^2 \alpha &= \frac{\tan^2 \alpha}{1 + \tan^2 \alpha} = \frac{\left(\frac{1}{2} \frac{\lambda_{h\psi}}{\Lambda_\psi} v_0^2 \sin \theta \right)^2}{\left(\mu_\psi + \frac{1}{2} \frac{\lambda_{h\psi}}{\Lambda_\psi} v_0^2 \cos \theta \right)^2 + \left(\frac{1}{2} \frac{\lambda_{h\psi}}{\Lambda_\psi} v_0^2 \sin \theta \right)^2}. \end{aligned}$$

After EWSB and the field rotation, we define the mass m_ψ as the coefficient of the term $-\bar{\psi}\psi$.

Using Eq. (A2), m_ψ is given by

$$\begin{aligned} m_\psi &= \mu_\psi \cos \alpha + \frac{1}{2} \frac{\lambda_{h\psi}}{\Lambda_\psi} v_0^2 \cos \xi = \mu_\psi \cos \alpha + \frac{1}{2} \frac{\lambda_{h\psi}}{\Lambda_\psi} v_0^2 (\cos \alpha \cos \theta - \sin \alpha \sin \theta), \\ &= \left[\mu_\psi + \frac{1}{2} \frac{\lambda_{h\psi}}{\Lambda_\psi} v_0^2 (\cos \theta - \tan \alpha \sin \theta) \right] \cos \alpha. \end{aligned}$$

Making use of the expression for $\tan \alpha$, m_ψ expands to

$$m_\psi = \left[\frac{\left(\mu_\psi + \frac{1}{2} \frac{\lambda_{h\psi}}{\Lambda_\psi} v_0^2 \cos \theta \right)^2 + \left(\frac{1}{2} \frac{\lambda_{h\psi}}{\Lambda_\psi} v_0^2 \sin \theta \right)^2}{\mu_\psi + \frac{1}{2} \frac{\lambda_{h\psi}}{\Lambda_\psi} v_0^2 \cos \theta} \right] \cos \alpha.$$

Squaring both sides of the above equation and using the relation for $\cos^2 \alpha$ gives the desired expression for the DM mass

$$\begin{aligned} m_\psi^2 &= \left[\frac{\left(\mu_\psi + \frac{1}{2} \frac{\lambda_{h\psi}}{\Lambda_\psi} v_0^2 \cos \theta \right)^2 + \left(\frac{1}{2} \frac{\lambda_{h\psi}}{\Lambda_\psi} v_0^2 \sin \theta \right)^2}{\mu_\psi + \frac{1}{2} \frac{\lambda_{h\psi}}{\Lambda_\psi} v_0^2 \cos \theta} \right]^2 \cos^2 \alpha = \frac{\left[\left(\mu_\psi + \frac{1}{2} \frac{\lambda_{h\psi}}{\Lambda_\psi} v_0^2 \cos \theta \right)^2 + \left(\frac{1}{2} \frac{\lambda_{h\psi}}{\Lambda_\psi} v_0^2 \sin \theta \right)^2 \right]^2}{\left(\mu_\psi + \frac{1}{2} \frac{\lambda_{h\psi}}{\Lambda_\psi} v_0^2 \cos \theta \right)^2 + \left(\frac{1}{2} \frac{\lambda_{h\psi}}{\Lambda_\psi} v_0^2 \sin \theta \right)^2} \\ &= \left(\mu_\psi + \frac{1}{2} \frac{\lambda_{h\psi}}{\Lambda_\psi} v_0^2 \cos \theta \right)^2 + \left(\frac{1}{2} \frac{\lambda_{h\psi}}{\Lambda_\psi} v_0^2 \sin \theta \right)^2. \end{aligned}$$

The signs of m_ψ , $\cos \alpha$ and $\sin \alpha$ are common; hence, we choose the common sign to be “+” for m_ψ , $\cos \alpha = +\sqrt{\cos^2 \alpha}$ and $\sin \alpha = \sqrt{\sin^2 \alpha}$. Therefore, the mass after EWSB is

$$m_\psi = \sqrt{\left(\mu_\psi + \frac{1}{2} \frac{\lambda_{h\psi}}{\Lambda_\psi} v_0^2 \cos \theta \right)^2 + \left(\frac{1}{2} \frac{\lambda_{h\psi}}{\Lambda_\psi} v_0^2 \sin \theta \right)^2}. \quad (\text{A5})$$

With the sign convention chosen above, expressions for $\cos \alpha$ and $\sin \alpha$ are given by

$$\begin{aligned}\cos \xi &= \cos \alpha (\cos \theta - \sin \theta \tan \alpha) = \frac{\mu_\psi \cos \theta + \frac{1}{2} \frac{\lambda_{h\psi}}{\Lambda_\psi} v_0^2}{\sqrt{\left(\mu_\psi + \frac{1}{2} \frac{\lambda_{h\psi}}{\Lambda_\psi} v_0^2 \cos \theta\right)^2 + \left(\frac{1}{2} \frac{\lambda_{h\psi}}{\Lambda_\psi} v_0^2 \sin \theta\right)^2}} \\ &= \frac{\mu_\psi}{m_\psi} \left(\cos \theta + \frac{1}{2} \frac{\lambda_{h\psi}}{\Lambda_\psi} \frac{v_0^2}{\mu_\psi} \right) \\ \sin \xi &= \cos \alpha (\sin \theta + \cos \theta \tan \alpha) = \frac{\mu_\psi \sin \theta}{\sqrt{\left(\mu_\psi + \frac{1}{2} \frac{\lambda_{h\psi}}{\Lambda_\psi} v_0^2 \cos \theta\right)^2 + \left(\frac{1}{2} \frac{\lambda_{h\psi}}{\Lambda_\psi} v_0^2 \sin \theta\right)^2}} \\ &= \frac{\mu_\psi}{m_\psi} \sin \theta\end{aligned}$$

where we have used Eq. (A5) to simplify the expression. Therefore, the final Lagrangian after EWSB and field redefinition becomes

$$\mathcal{L}_\psi = \mathcal{L}_{\text{SM}} + \bar{\psi} i \not{\partial} \psi - m_\psi \bar{\psi} \psi - \frac{\lambda_{h\psi}}{\Lambda_\psi} \left[\cos \xi \bar{\psi} \psi + \sin \xi \bar{\psi} i \gamma_5 \psi \right] \left(v_0 h + \frac{1}{2} h^2 \right),$$

where

$$\cos \xi = \frac{\mu_\psi}{m_\psi} \left(\cos \theta + \frac{1}{2} \frac{\lambda_{h\psi}}{\Lambda_\psi} \frac{v_0^2}{\mu_\psi} \right) \quad \text{and} \quad \sin \xi = \frac{\mu_\psi}{m_\psi} \sin \theta.$$

2. Majorana fermion model

Consider the Majorana fermion DM field χ Lagrangian after EWSB of

$$\begin{aligned}\mathcal{L}_\chi &= \mathcal{L}_{\text{SM}} + \frac{1}{2} \bar{\chi} i \not{\partial} \chi - \frac{1}{2} \left[\mu_\chi \bar{\chi} \chi + \frac{1}{2} \frac{\lambda_{h\chi}}{\Lambda_\chi} v_0^2 \left(\cos \theta \bar{\chi} \chi + \sin \theta \bar{\chi} i \gamma_5 \chi \right) \right] \\ &\quad - \frac{1}{2} \frac{\lambda_{h\chi}}{\Lambda_\chi} \left(\cos \theta \bar{\chi} \chi + \sin \theta \bar{\chi} i \gamma_5 \chi \right) \left(v_0 h + \frac{1}{2} h^2 \right).\end{aligned}$$

With the conventional factor of $1/2$ in front of each Majorana field bilinear, the form of the Majorana model Lagrangian after EWSB and chiral rotation is analogous to that of the Dirac model. The proper chiral rotation is again given by

$$\tan \alpha = \left(-\frac{1}{2} \frac{\lambda_{h\chi}}{\Lambda_\chi} v_0^2 \sin \theta \right) \left(\mu_\chi + \frac{1}{2} \frac{\lambda_{h\chi}}{\Lambda_\chi} v_0^2 \cos \theta \right)^{-1},$$

which leads to a real DM mass m_χ of

$$m_\chi = \sqrt{\left(\mu_\chi + \frac{1}{2} \frac{\lambda_{h\chi}}{\Lambda_\chi} v_0^2 \cos \theta \right)^2 + \left(\frac{1}{2} \frac{\lambda_{h\chi}}{\Lambda_\chi} v_0^2 \sin \theta \right)^2}.$$

Finally, the Majorana fermion Lagrangian after EWSB and chiral rotation is given by

$$\mathcal{L}_\chi = \mathcal{L}_{\text{SM}} + \frac{1}{2} \bar{\chi} i \not{\partial} \chi - \frac{1}{2} m_\chi \bar{\chi} \chi - \frac{1}{2} \frac{\lambda_{h\chi}}{\Lambda_\chi} \left[\cos \xi \bar{\chi} \chi + \sin \xi \bar{\chi} i \gamma_5 \chi \right] \left(v_0 h + \frac{1}{2} h^2 \right),$$

where

$$\cos \xi = \frac{\mu_\chi}{m_\chi} \left(\cos \theta + \frac{1}{2} \frac{\lambda_{h\chi}}{\Lambda_\chi} \frac{v_0^2}{\mu_\chi} \right) \quad \text{and} \quad \sin \xi = \frac{\mu_\chi}{m_\chi} \sin \theta.$$

as stated for the Majorana fermion model in Section. II.

-
- [1] F. Zwicky, *On the Masses of Nebulae and of Clusters of Nebulae*, *Astrophys. J* **86** (1937) 217.
 - [2] L. Bergstrom, *Nonbaryonic dark matter: Observational evidence and detection methods*, *Rept. Prog. Phys.* **63** (2000) 793, [[hep-ph/0002126](#)].
 - [3] G. Bertone, D. Hooper, and J. Silk, *Particle dark matter: Evidence, candidates and constraints*, *Phys. Rept.* **405** (2005) 279–390, [[hep-ph/0404175](#)].
 - [4] B. Patt and F. Wilczek, *Higgs-field portal into hidden sectors*, [hep-ph/0605188](#).
 - [5] Y. G. Kim and K. Y. Lee, *The Minimal model of fermionic dark matter*, *Phys. Rev.* **D75** (2007) 115012, [[hep-ph/0611069](#)].
 - [6] V. Barger, P. Langacker, M. McCaskey, M. J. Ramsey-Musolf, and G. Shaughnessy, *LHC Phenomenology of an Extended Standard Model with a Real Scalar Singlet*, *Phys. Rev.* **D77** (2008) 035005, [[arXiv:0706.4311](#)].
 - [7] Y. G. Kim, K. Y. Lee, and S. Shin, *Singlet fermionic dark matter*, *JHEP* **05** (2008) 100, [[arXiv:0803.2932](#)].
 - [8] J.-H. Yu, *Vector Fermion-Portal Dark Matter: Direct Detection and Galactic Center Gamma-Ray Excess*, *Phys. Rev.* **D90** (2014), no. 9 095010, [[arXiv:1409.3227](#)].
 - [9] S. Kanemura, S. Matsumoto, T. Nabeshima, and N. Okada, *Can WIMP Dark Matter overcome the Nightmare Scenario?*, *Phys. Rev.* **D82** (2010) 055026, [[arXiv:1005.5651](#)].
 - [10] I. Low, P. Schwaller, G. Shaughnessy, and C. E. M. Wagner, *The dark side of the Higgs boson*, *Phys. Rev.* **D85** (2012) 015009, [[arXiv:1110.4405](#)].
 - [11] C. Englert, T. Plehn, M. Rauch, D. Zerwas, and P. M. Zerwas, *LHC: Standard Higgs and Hidden Higgs*, *Phys. Lett.* **B707** (2012) 512–516, [[arXiv:1112.3007](#)].
 - [12] B. Batell, S. Gori, and L.-T. Wang, *Exploring the Higgs Portal with 10/fb at the LHC*, *JHEP* **06** (2012) 172, [[arXiv:1112.5180](#)].
 - [13] P. J. Fox, R. Harnik, J. Kopp, and Y. Tsai, *Missing Energy Signatures of Dark Matter at the LHC*, *Phys. Rev.* **D85** (2012) 056011, [[arXiv:1109.4398](#)].
 - [14] O. Lebedev, H. M. Lee, and Y. Mambrini, *Vector Higgs-portal dark matter and the invisible Higgs*, *Phys. Lett.* **B707** (2012) 570–576, [[arXiv:1111.4482](#)].
 - [15] Y. Mambrini, *Higgs searches and singlet scalar dark matter: Combined constraints from XENON 100 and the LHC*, *Phys. Rev.* **D84** (2011) 115017, [[arXiv:1108.0671](#)].
 - [16] M. Pospelov and A. Ritz, *Higgs decays to dark matter: beyond the minimal model*, *Phys. Rev.* **D84** (2011) 113001, [[arXiv:1109.4872](#)].

- [17] C. Englert, T. Plehn, D. Zerwas, and P. M. Zerwas, *Exploring the Higgs portal*, *Phys. Lett.* **B703** (2011) 298–305, [[arXiv:1106.3097](#)].
- [18] J. F. Kamenik and C. Smith, *Could a light Higgs boson illuminate the dark sector?*, *Phys. Rev.* **D85** (2012) 093017, [[arXiv:1201.4814](#)].
- [19] J. M. Cline and K. Kainulainen, *Electroweak baryogenesis and dark matter from a singlet Higgs*, *JCAP* **1301** (2013) 012, [[arXiv:1210.4196](#)].
- [20] Y. Farzan and A. R. Akbarieh, *VDM: A model for Vector Dark Matter*, *JCAP* **1210** (2012) 026, [[arXiv:1207.4272](#)].
- [21] H.-C. Tsai and K.-C. Yang, *Dark Matter Mass Constrained by the Relic Abundance, Direct Detections, and Colliders*, *Phys. Rev.* **D87** (2013), no. 11 115016, [[arXiv:1301.4186](#)].
- [22] A. Greljo, J. Julio, J. F. Kamenik, C. Smith, and J. Zupan, *Constraining Higgs mediated dark matter interactions*, *JHEP* **11** (2013) 190, [[arXiv:1309.3561](#)].
- [23] D. G. E. Walker, *Unitarity Constraints on Higgs Portals*, [arXiv:1310.1083](#).
- [24] L. Carpenter, A. DiFranzo, M. Mulhearn, C. Shimmin, S. Tulin, and D. Whiteson, *Mono-Higgs-boson: A new collider probe of dark matter*, *Phys. Rev.* **D89** (2014), no. 7 075017, [[arXiv:1312.2592](#)].
- [25] K. R. Dienes, J. Kumar, B. Thomas, and D. Yaylali, *Overcoming Velocity Suppression in Dark-Matter Direct-Detection Experiments*, *Phys. Rev.* **D90** (2014), no. 1 015012, [[arXiv:1312.7772](#)].
- [26] G. Busoni, A. De Simone, E. Morgante, and A. Riotto, *On the Validity of the Effective Field Theory for Dark Matter Searches at the LHC*, *Phys.Lett.* **B728** (2014) 412–421, [[arXiv:1307.2253](#)].
- [27] N. Craig, H. K. Lou, M. McCullough, and A. Thalappilil, *The Higgs Portal Above Threshold*, [arXiv:1412.0258](#).
- [28] P. Ko, W.-I. Park, and Y. Tang, *Higgs-Portal Dark Matter for GeV Gamma-Ray Excess*, in *2nd Toyama International Workshop on Higgs as a Probe of ew Physics (HPNP2015) Toyama, Japan, February 11-15, 2015*, 2015. [arXiv:1504.06944](#).
- [29] S. Baek, P. Ko, and W.-I. Park, *Invisible Higgs Decay Width vs. Dark Matter Direct Detection Cross Section in Higgs Portal Dark Matter Models*, *Phys. Rev.* **D90** (2014), no. 5 055014, [[arXiv:1405.3530](#)].
- [30] K. Ghorbani, *Fermionic dark matter with pseudo-scalar Yukawa interaction*, *JCAP* **1501** (2015) 015, [[arXiv:1408.4929](#)].
- [31] P. Ko, W.-I. Park, and Y. Tang, *Higgs portal vector dark matter for GeV scale γ -ray excess from galactic center*, *JCAP* **1409** (2014) 013, [[arXiv:1404.5257](#)].
- [32] M. Duerr, P. Fileviez Perez, and J. Smirnov, *Scalar Singlet Dark Matter and Gamma Lines*, *Phys. Lett.* **B751** (2015) 119–122, [[arXiv:1508.04418](#)].
- [33] H. Han and S. Zheng, *Higgs-portal Scalar Dark Matter: Scattering Cross Section and Observable Limits*, [arXiv:1510.06165](#).

- [34] M. Duerr, P. F. Perez, and J. Smirnov, *Scalar Dark Matter: Direct vs. Indirect Detection*, [arXiv:1509.04282](#).
- [35] F. S. Queiroz, K. Sinha, and A. Strumia, *Leptoquarks, Dark Matter, and Anomalous LHC Events*, *Phys. Rev.* **D91** (2015), no. 3 035006, [[arXiv:1409.6301](#)].
- [36] **ATLAS Collaboration**, G. Aad et al., *Observation of a new particle in the search for the Standard Model Higgs boson with the ATLAS detector at the LHC*, *Phys. Lett.* **B716** (2012) 1–29, [[arXiv:1207.7214](#)].
- [37] **CMS Collaboration**, S. Chatrchyan et al., *Observation of a new boson at a mass of 125 GeV with the CMS experiment at the LHC*, *Phys. Lett.* **B716** (2012) 30–61, [[arXiv:1207.7235](#)].
- [38] E. A. Baltz, M. Battaglia, M. E. Peskin, and T. Wizansky, *Determination of dark matter properties at high-energy colliders*, *Phys. Rev.* **D74** (2006) 103521, [[hep-ph/0602187](#)].
- [39] J. M. Cline, K. Kainulainen, P. Scott, and C. Weniger, *Update on scalar singlet dark matter*, *Phys. Rev.* **D88** (2013) 055025, [[arXiv:1306.4710](#)]. [Erratum: *Phys. Rev.* D92, no. 3, 039906 (2015)].
- [40] K. Cheung, Y.-L. S. Tsai, P.-Y. Tseng, T.-C. Yuan, and A. Zee, *Global Study of the Simplest Scalar Phantom Dark Matter Model*, *JCAP* **1210** (2012) 042, [[arXiv:1207.4930](#)].
- [41] A. Djouadi, O. Lebedev, Y. Mambrini, and J. Quevillon, *Implications of LHC searches for Higgs–portal dark matter*, *Phys.Lett.* **B709** (2012) 65–69, [[arXiv:1112.3299](#)].
- [42] M. Endo and Y. Takaesu, *Heavy WIMP through Higgs portal at the LHC*, *Phys.Lett.* **B743** (2015) 228–234, [[arXiv:1407.6882](#)].
- [43] A. Djouadi, A. Falkowski, Y. Mambrini, and J. Quevillon, *Direct Detection of Higgs-Portal Dark Matter at the LHC*, *Eur. Phys. J.* **C73** (2013), no. 6 2455, [[arXiv:1205.3169](#)].
- [44] H. Han and S. Zheng, *New Constraints on Higgs-portal Scalar Dark Matter*, [arXiv:1509.01765](#).
- [45] A. Urbano and W. Xue, *Constraining the Higgs portal with antiprotons*, *JHEP* **03** (2015) 133, [[arXiv:1412.3798](#)].
- [46] L. Lopez-Honorez, T. Schwetz, and J. Zupan, *Higgs portal, fermionic dark matter, and a Standard Model like Higgs at 125 GeV*, *Phys. Lett.* **B716** (2012) 179–185, [[arXiv:1203.2064](#)].
- [47] M. A. Fedderke, J.-Y. Chen, E. W. Kolb, and L.-T. Wang, *The Fermionic Dark Matter Higgs Portal: an effective field theory approach*, *JHEP* **08** (2014) 122, [[arXiv:1404.2283](#)].
- [48] V. Silveira and A. Zee, *Scalar phantoms*, *Phys. Lett. B* **161** (1985), no. 13 136 – 140.
- [49] J. McDonald, *Gauge singlet scalars as cold dark matter*, *Phys. Rev. D* **50** (1994) 3637–3649.
- [50] C. P. Burgess, M. Pospelov, and T. ter Veldhuis, *The Minimal model of nonbaryonic dark matter: A Singlet scalar*, *Nucl. Phys.* **B619** (2001) 709–728, [[hep-ph/0011335](#)].
- [51] S. Baek, P. Ko, W.-I. Park, and E. Senaha, *Higgs Portal Vector Dark Matter : Revisited*, *JHEP* **1305** (2013) 036, [[arXiv:1212.2131](#)].
- [52] M. Duch, B. Grzadkowski, and M. McGarrie, *A stable Higgs portal with vector dark matter*, *JHEP* **09** (2015) 162, [[arXiv:1506.08805](#)].

- [53] S. Baek, P. Ko, and W.-I. Park, *Search for the Higgs portal to a singlet fermionic dark matter at the LHC*, *JHEP* **1202** (2012) 047, [[arXiv:1112.1847](#)].
- [54] M. Gonderinger, H. Lim, and M. J. Ramsey-Musolf, *Complex Scalar Singlet Dark Matter: Vacuum Stability and Phenomenology*, *Phys. Rev.* **D86** (2012) 043511, [[arXiv:1202.1316](#)].
- [55] M. Gonderinger, Y. Li, H. Patel, and M. J. Ramsey-Musolf, *Vacuum Stability, Perturbativity, and Scalar Singlet Dark Matter*, *JHEP* **01** (2010) 053, [[arXiv:0910.3167](#)].
- [56] M. Kadastik, K. Kannike, A. Racioppi, and M. Raidal, *Implications of the 125 GeV Higgs boson for scalar dark matter and for the CMSSM phenomenology*, *JHEP* **05** (2012) 061, [[arXiv:1112.3647](#)].
- [57] N. Khan and S. Rakshit, *Study of electroweak vacuum metastability with a singlet scalar dark matter*, *Phys. Rev.* **D90** (2014), no. 11 113008, [[arXiv:1407.6015](#)].
- [58] R. N. Lerner and J. McDonald, *Gauge singlet scalar as inflaton and thermal relic dark matter*, *Phys. Rev.* **D80** (2009) 123507, [[arXiv:0909.0520](#)].
- [59] Z.-z. Xing, H. Zhang, and S. Zhou, *Impacts of the Higgs mass on vacuum stability, running fermion masses and two-body Higgs decays*, *Phys. Rev.* **D86** (2012) 013013, [[arXiv:1112.3112](#)].
- [60] J. Elias-Miro, J. R. Espinosa, G. F. Giudice, G. Isidori, A. Riotto, and A. Strumia, *Higgs mass implications on the stability of the electroweak vacuum*, *Phys. Lett.* **B709** (2012) 222–228, [[arXiv:1112.3022](#)].
- [61] **Planck Collaboration**, P. Ade et al., *Planck 2013 results. XVI. Cosmological parameters*, *Astron.Astrophys.* **571** (2014) A16, [[arXiv:1303.5076](#)].
- [62] A. Semenov, *LanHEP - a package for automatic generation of Feynman rules from the Lagrangian*. Updated version 3.2, [arXiv:1412.5016](#).
- [63] A. Semenov, *LanHEP: A Package for the automatic generation of Feynman rules in field theory*. Version 3.0, *Comput.Phys.Commun.* **180** (2009) 431–454, [[arXiv:0805.0555](#)].
- [64] G. Belanger, F. Boudjema, A. Pukhov, and A. Semenov, *micrOMEGAs_3: A program for calculating dark matter observables*, *Comput.Phys.Commun.* **185** (2014) 960–985, [[arXiv:1305.0237](#)].
- [65] G. Belanger, F. Boudjema, and A. Pukhov, *micrOMEGAs : a code for the calculation of Dark Matter properties in generic models of particle interaction*, in *The Dark Secrets of the Terascale*, pp. 739–790, 2013. [arXiv:1402.0787](#).
- [66] R. P. Brent, *Algorithms for Minimisation Without Derivatives*. Prentice Hall, 1973.
- [67] G. Belanger, B. Dumont, U. Ellwanger, J. Gunion, and S. Kraml, *Global fit to Higgs signal strengths and couplings and implications for extended Higgs sectors*, *Phys. Rev.* **D88** (2013) 075008, [[arXiv:1306.2941](#)].
- [68] M. E. Peskin, *Comparison of LHC and ILC Capabilities for Higgs Boson Coupling Measurements*, [arXiv:1207.2516](#).
- [69] **LHC Higgs Cross Section Working Group**, S. Dittmaier et al., *Handbook of LHC Higgs Cross Sections: 1. Inclusive Observables*, [arXiv:1101.0593](#).

- [70] W. B. Atwood, A. A. Abdo, M. Ackermann, W. Althouse, B. Anderson, M. Axelsson, L. Baldini, J. Ballet, D. L. Band, and G. Barbiellini et al., *The Large Area Telescope on the Fermi Gamma-Ray Space Telescope Mission*, *Astrophys. J.* **697** (2009) 1071–1102, [[arXiv:0902.1089](#)].
- [71] A. Abramowski et al., *Search for a Dark Matter Annihilation Signal from the Galactic Center Halo with H.E.S.S.*, *Phys. Rev. Lett.* **106** (2011), no. 16 161301, [[arXiv:1103.3266](#)].
- [72] C. Claudio for the AMS Collaboration, *The cosmic ray electron and positron spectra measured by AMS-02*, in *10th International Symposium on Cosmology and Particle Astrophysics (CosPA 2013) Honolulu, Hawaii, USA, November 12-15, 2013*, 2014. [arXiv:1402.0437](#).
- [73] R. M. Wagner, E. J. Lindfors, A. Sillanpää, and S. Wagner for the CTA Consortium, *The CTA Observatory*, *ArXiv e-prints* (2009) [[arXiv:0912.3742](#)].
- [74] J. M. Cline and P. Scott, *Dark Matter CMB Constraints and Likelihoods for Poor Particle Physicists*, *JCAP* **1303** (2013) 044, [[arXiv:1301.5908](#)].
- [75] D. P. Finkbeiner, S. Galli, T. Lin, and T. R. Slatyer, *Searching for Dark Matter in the CMB: A Compact Parameterization of Energy Injection from New Physics*, *Phys. Rev.* **D85** (2012) 043522, [[arXiv:1109.6322](#)].
- [76] T. R. Slatyer, *Energy Injection And Absorption In The Cosmic Dark Ages*, *Phys. Rev.* **D87** (2013), no. 12 123513, [[arXiv:1211.0283](#)].
- [77] E. Komatsu et al., *Seven-year Wilkinson Microwave Anisotropy Probe (WMAP) Observations: Cosmological Interpretation*, *Astrophys. J.* **192** (2011) 18, [[arXiv:1001.4538](#)].
- [78] T. R. Slatyer, *Indirect Dark Matter Signatures in the Cosmic Dark Ages I. Generalizing the Bound on s-wave Dark Matter Annihilation from Planck*, [arXiv:1506.03811](#).
- [79] **Fermi-LAT Collaboration**, M. Ackermann et al., *Search for gamma-ray spectral lines with the Fermi large area telescope and dark matter implications*, *Phys. Rev.* **D88** (2013) 082002, [[arXiv:1305.5597](#)].
- [80] **Fermi-LAT Collaboration**, M. Ackermann et al., *Searching for Dark Matter Annihilation from Milky Way Dwarf Spheroidal Galaxies with Six Years of Fermi-LAT Data*, [arXiv:1503.02641](#).
- [81] J. Aleksić et al., *Performance of the MAGIC stereo system obtained with Crab Nebula data*, *AstroPhys.* **35** (2012) 435–448, [[arXiv:1108.1477](#)].
- [82] **HESS Collaboration**, F. Aharonian et al., *Observations of the Crab Nebula with H.E.S.S.*, *Astron. Astrophys.* **457** (2006) 899–915, [[astro-ph/0607333](#)].
- [83] J. Holder et al., *Status of the VERITAS Observatory*, *AIP Conf. Proc.* **1085** (2009) 657–660, [[arXiv:0810.0474](#)].
- [84] K. Bernlöhner et al., *Monte Carlo design studies for the Cherenkov Telescope Array*, *Astroparticle Physics* **43** (2013) 171–188, [[arXiv:1210.3503](#)].
- [85] M. Doro et al., *Dark matter and fundamental physics with the Cherenkov Telescope Array*, *Astroparticle Physics* **43** (2013) 189–214, [[arXiv:1208.5356](#)].

- [86] M. Pierre, J. M. Siegal-Gaskins, and P. Scott, *Sensitivity of CTA to dark matter signals from the Galactic Center*, *JCAP* **1406** (2014) 024, [[arXiv:1401.7330](#)]. [Erratum: *JCAP* 1410, E01 (2014)].
- [87] H. Silverwood, C. Weniger, P. Scott, and G. Bertone, *A realistic assessment of the CTA sensitivity to dark matter annihilation*, *JCAP* **1503** (2015), no. 03 055, [[arXiv:1408.4131](#)].
- [88] M. Doro et al., *Dark matter and fundamental physics with the Cherenkov Telescope Array*, *Astroparticle Physics* **43** (2013) 189–214, [[arXiv:1208.5356](#)].
- [89] M. Actis et al., *Design concepts for the Cherenkov Telescope Array CTA: an advanced facility for ground-based high-energy gamma-ray astronomy*, *Experimental Astronomy* **32** (2011) 193–316, [[arXiv:1008.3703](#)].
- [90] J. F. Navarro, E. Hayashi, C. Power, A. Jenkins, C. S. Frenk, S. D. M. White, V. Springel, J. Stadel, and T. R. Quinn, *The Inner structure of Lambda-CDM halos 3: Universality and asymptotic slopes*, *Mon. Not. Roy. Astron. Soc.* **349** (2004) 1039, [[astro-ph/0311231](#)].
- [91] L. Pieri, J. Lavalle, G. Bertone, and E. Branchini, *Implications of high-resolution simulations on indirect dark matter searches*, *Phys. Rev. D* **83** (2011), no. 2 023518, [[arXiv:0908.0195](#)].
- [92] J. F. Navarro, C. S. Frenk, and S. D. M. White, *A Universal density profile from hierarchical clustering*, *Astrophys. J.* **490** (1997) 493–508, [[astro-ph/9611107](#)].
- [93] D. G. Cerdeño and A. M. Green, *Direct detection of WIMPs*, in *Particle Dark Matter : Observations, Models and Searches* (G. Bertone, ed.), p. 347. Cambridge University Press, 2010.
- [94] K. Freese, M. Lisanti, and C. Savage, *Colloquium: Annual modulation of dark matter*, *Rev. Mod. Phys.* **85** (2013) 1561–1581, [[arXiv:1209.3339](#)].
- [95] P. Gondolo, *Phenomenological introduction to direct dark matter detection*, in *Dark matter in cosmology, quantum measurements, experimental gravitation. Proceedings, 31st Rencontres de Moriond, 16th Moriond Workshop, Les Arcs, France, January 2-27, 1996*, 1996. [hep-ph/9605290](#).
- [96] A. Berlin, D. Hooper, and S. D. McDermott, *Simplified Dark Matter Models for the Galactic Center Gamma-Ray Excess*, *Phys. Rev. D* **89** (2014), no. 11 115022, [[arXiv:1404.0022](#)].
- [97] J. Lewin and P. Smith, *Review of mathematics, numerical factors, and corrections for dark matter experiments based on elastic nuclear recoil*, *Astroparticle Physics* **6** (1996), no. 1 87 – 112.
- [98] G. Duda, A. Kemper, and P. Gondolo, *Model Independent Form Factors for Spin Independent Neutralino-Nucleon Scattering from Elastic Electron Scattering Data*, *JCAP* **0704** (2007) 012, [[hep-ph/0608035](#)].
- [99] Y. Akrami, C. Savage, P. Scott, J. Conrad, and J. Edsjö, *How well will ton-scale dark matter direct detection experiments constrain minimal supersymmetry?*, *JCAP* **4** (2011) 12, [[arXiv:1011.4318](#)].
- [100] J. M. Alarcon, J. Martin Camalich, and J. A. Oller, *The chiral representation of the πN scattering amplitude and the pion-nucleon sigma term*, *Phys. Rev. D* **85** (2012) 051503, [[arXiv:1110.3797](#)].
- [101] M. Shifman, A. Vainshtein, and V. Zakharov, *Remarks on higgs-boson interactions with nucleons*, *Phys. Lett. B* **78** (1978), no. 4 443 – 446.

- [102] E. Aprile for the XENON1T collaboration, *The XENON1T Dark Matter Search Experiment*, *ArXiv e-prints* (2012) [[arXiv:1206.6288](#)].
- [103] **XENON Collaboration**, P. Beltrame et al., *Direct Dark Matter search with the XENON program*, in *Proceedings, 48th Rencontres de Moriond on Electroweak Interactions and Unified Theories*, pp. 143–148, 2013. [arXiv:1305.2719](#).
- [104] **XENON**, E. Aprile et al., *Physics reach of the XENON1T dark matter experiment*, *Submitted to: JCAP* (2015) [[arXiv:1512.07501](#)].
- [105] **XENON100 Collaboration**, E. Aprile et al., *Dark Matter Results from 225 Live Days of XENON100 Data*, *Phys. Rev. Lett.* **109** (2012) 181301, [[arXiv:1207.5988](#)].
- [106] M. Woods for the LUX Collaboration, *Underground Commissioning of LUX*, in *Proceedings, 48th Rencontres de Moriond on Very High Energy Phenomena in the Universe*, pp. 211–214, 2013. [arXiv:1306.0065](#).
- [107] S. Fiorucci for the LUX Collaboration, *The LUX Dark Matter Search - Status Update*, *Journal of Physics Conference Series* **460** (2013), no. 1 012005, [[arXiv:1301.6942](#)].
- [108] G. J. Feldman and R. D. Cousins, *A Unified approach to the classical statistical analysis of small signals*, *Phys. Rev.* **D57** (1998) 3873–3889, [[physics/9711021](#)].
- [109] C. Savage, A. Scaffidi, M. White, and A. G. Williams, *LUX likelihood and limits on spin-independent and spin-dependent WIMP couplings with LUXCalc*, *Phys. Rev.* **D92** (2015), no. 10 103519, [[arXiv:1502.02667](#)].
- [110] **LUX Collaboration**, D. Akerib et al., *First results from the LUX dark matter experiment at the Sanford Underground Research Facility*, *Phys. Rev. Lett.* **112** (2014), no. 9 091303, [[arXiv:1310.8214](#)].
- [111] C. Savage et al., “TPCMC: a Time Projection Chamber Monte Carlo for dark matter searches.” In preparation.
- [112] M. Szydagis, N. Barry, K. Kazkaz, J. Mock, D. Stolp, et al., *NEST: A Comprehensive Model for Scintillation Yield in Liquid Xenon*, *JINST* **6** (2011) P10002, [[arXiv:1106.1613](#)].
- [113] M. Szydagis, A. Fyhrie, D. Thorngren, and M. Tripathi, *Enhancement of NEST Capabilities for Simulating Low-Energy Recoils in Liquid Xenon*, *JINST* **8** (2013) C10003, [[arXiv:1307.6601](#)].